Physics of Fluids

RESEARCH ARTICLE | JANUARY 09 2023

Finite-wing-analogy formula for compressibility correction to pressure coefficient of an underwater vehicle model at low Mach number

Yu Wang (汪宇) ; Yi Liu (刘毅); Zhiteng Zhou (周志腾) ; Shizhao Wang (王士召)

Check for updates

Physics of Fluids 35, 016111 (2023)
https://doi.org/10.1063/5.0129637

View Online
Export Citation

08 April 2024 03:18:05

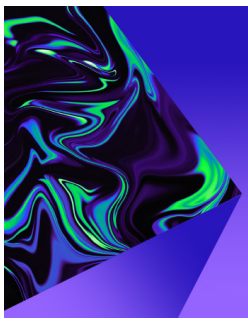
Physics of Fluids
Special Topic:
Selected Papers from the 2023 Non-Newtonian Fluid Mechanics Symposium in China
Submit Today
AIP Publishing

AIP Publishing

Physics of Fluids ARTICLE scitation.org/journal/phf

Finite-wing-analogy formula for compressibility correction to pressure coefficient of an underwater vehicle model at low Mach number

Cite as: Phys. Fluids **35**, 016111 (2023); doi: 10.1063/5.0129637
Submitted: 6 October 2022 · Accepted: 16 December 2022 ·
Published Online: 9 January 2023

View Online Export Citation CrossMark

Yu Wang (汪宇),[1,2] Yi Liu (刘毅),[1,2] Zhiteng Zhou (周志腾),[1,2] and Shizhao Wang (王士召)[1,2,a)]

AFFILIATIONS

[1]The State Key Laboratory of Nonlinear Mechanics, Institute of Mechanics, Chinese Academy of Sciences, Beijing 100190, China
[2]School of Engineering Sciences, University of Chinese Academy of Sciences, Beijing 101408, China

[a)]Author to whom correspondence should be addressed: wangsz@lnm.imech.ac.cn

ABSTRACT

Wind tunnels are usually used to investigate the flows and forces associated with underwater vehicles when free-surface effects can be ignored. However, because of the large differences between air and water in density and viscosity, the freestream Mach number in a wind tunnel is much higher than that in a water tunnel or towing tank at the same Reynolds number. Therefore, compressibility correction is required for accurate measurement compatibility between wind tunnels and water tunnels or towing tanks. In the study reported here, the flows and forces associated with an underwater vehicle model at different Mach numbers were investigated by solving the Navier–Stokes equations for compressible flow numerically as virtual-wind tunnel experiments. The freestream Mach number Ma varies from 0.004 to 0.5. The distribution of the pressure coefficient on the hull and the effects of Ma on the peaks of the pressure coefficient are discussed in detail. The performances of the Prandtl–Glauert rule, the Karman–Tsien rule, and the Laitone rule for compressibility correction to the pressure coefficient of underwater vehicles are assessed. Defining the average correction factor with larger values for better correction effect, the values for these three compressibility correction formulas are 0.51, 0.38, and 0.23, respectively. A finite-wing-analogy formula to improve the compressibility correction to the pressure coefficient at low Ma is proposed. Inspired by the finite-wing correction to the lift slope of airfoils, the proposed formula offers good convergence of the pressure coefficient and highly accurate compressibility correction with an average correction factor of 0.84.

Published under an exclusive license by AIP Publishing. https://doi.org/10.1063/5.0129637

NOMENCLATURE

a_0	Lift slope in incompressible flow
$a_{0,comp}$	Lift slope in compressible flow
$a_1, \beta^*, \sigma_k, \beta, \sigma_\omega, \gamma$	SST model constants
AR	Aspect ratio
c	Local sound speed
C_p	Pressure coefficient in compressible flow
$C_{p,0}$	Pressure coefficient in incompressible flow
D	Maximum diameter of SUBOFF
E	Total energy
e	Euler number
e	Internal enthalpy
H	Total enthalpy
k	Turbulent kinetic energy
L	Length of SUBOFF
Ma	Freestream Mach number
p	Pressure
p_∞	Freestream pressure
Pr_l	Laminar Prandtl number
Pr_t	Turbulent Prandtl number
Re_L	Reynolds number based on length
T	Temperature
t	Time
u_i, u_j	Velocity components
V_∞	Freestream velocity
W_{ij}	Rate-of-rotation tensor
x, y, z	Cartesian coordinates
γ_G	Specific heat ratio
δ_{ij}	Kronecker delta

08 April 2024 03:18:05

ε	Aspect-ratio analogy factor
ζ	Correction factor of finite-wing-analogy formula
η	Compressibility error
κ	Pressure-coefficient correction factor
μ	Molecular viscosity
μ_t	Turbulent eddy viscosity
ν	Kinematic viscosity
ξ	Average correction factor
ρ	Density
ρ_∞	Freestream density
τ_{ij}	Molecular stress tensor
τ_w	Wall shear stress
τ_{ij}^t	Reynolds stress tensor
Ω	Vorticity magnitude
ω	Specific dissipation rate
ω_y	Vorticity in Y direction

Subscripts

a, b, c, d	Typical location
cor	Before correction
For-I	Correction formula I
For-II	Correction formula II
KT	Karman–Tsien rule
Lai	Laitone rule
PG	Prandtl–Glauert rule
uncor	After correction

Abbreviations

DES	Detached eddy simulation
DNS	Direct numerical simulation
RANS	Reynolds-averaged Navier–Stokes

I. INTRODUCTION

The SUBOFF model due to the Defense Advanced Research Projects Agency is a body of revolution that is used widely in both wind tunnel and towing-tank experiments to study the fluid dynamics of underwater vehicles.[1] For example, Huang *et al.*[2] measured complex flows over SUBOFF in a wind tunnel for $Re_L = 1.2 \times 10^7$, and Roddy[3] explored the stability and control characteristics of different SUBOFF configurations in the David Taylor Model Basin. Liu *et al.*[4] evaluated the influence of support struts and the freestream in wind tunnels, Ashok *et al.*[5] conducted wind tunnel experiments for the wake of SUBOFF without appendages at large angles of attack, Jiménez *et al.*[6] studied the evolution of the wake of SUBOFF without appendages at different Reynolds numbers with a closed-loop wind tunnel, and Jiménez *et al.*[7] investigated the downstream of SUBOFF with fins in a wind tunnel. More experimental setups[8–17] used to investigate the flows and forces associated with SUBOFF are reported in Table I.

Many experiments on flows around underwater vehicles are conducted in wind tunnels when free-surface effects can be neglected, and a wind tunnel can be used as an alternative to a towing tank or water tunnel when dynamic similarity based on the Reynolds number *Re* is guaranteed.[18] However, the kinematic viscosities of air and water differ by an order of magnitude because of the large differences between their densities, dynamic viscosities, and other properties of air and water. Therefore, the freestream velocity in a wind tunnel is an order of magnitude greater than that in a water tunnel or towing tank for the same *Re*. This means that the Mach number *Ma* for the freestream velocity in a wind tunnel is much higher than that in a corresponding water tunnel or towing tank. For example, in the experiment conducted by Jiménez *et al.*,[6] the Mach number was estimated to have been as high as $Ma = 0.2$ for $Re_L = 1.2 \times 10^7$ with the static pressure varied from 5 to 218 atm. It is worth noting that the Mach number for the freestream velocity could have been as high as $Ma = 0.5$ with the static pressure is 1 atm. As shown in Table I, wind tunnel and water tunnel experiments are widely used in various studies of SUBOFF. However, the high Reynolds number of SUBOFF experiment is difficult to reach for a conventional water tunnel, while a wind tunnel can easily obtain. Moreover, the measurement of pressure coefficients in a water tunnel is more difficult than in a wind tunnel. Hence, a large number of SUBOFF pressure coefficient measurement experiments have been done in wind tunnels with high Mach numbers and compressibility effect that may not be negligible. Therefore, compressibility correction is required for accurate measurement compatibility between a wind tunnel and a water tunnel or towing tank.

TABLE I. Details of previous experiments to investigate flows and forces associated with SUBOFF model.

Year	Reference	Experimental equipment	Re_L
1990	Roddy[3]	Towing tank	1.4×10^7
1990	Kowalyshyn[8]	Towing tank	⋯
1990	Liu *et al.*[4]	Wind tunnel	1.2×10^7
1990	Blanton *et al.*[9]	Wind tunnel	⋯
1990	Gowing[10]	Wind tunnel	⋯
1990	Jiang *et al.*[11]	Wind tunnel	⋯
1994	Huang *et al.*[2]	Wind tunnel	1.2×10^7–3.5×10^7
2007	Hosder and Simpson[12]	Wind tunnel	4.5×10^7, 5.5×10^7
2010	Jiménez *et al.*[6]	Wind tunnel	1.1×10^6–6.7×10^7
2010	Jiménez *et al.*[7]	Wind tunnel	4.9×10^5–1.8×10^6
2015	Ashok *et al.*[5]	Wind tunnel	2.4×10^6–3.0×10^7
2015	Ashok *et al.*[13]	Wind tunnel	2.4×10^6
2018	Lin *et al.*[14]	Towing tank	1.2×10^7
2021	Liang *et al.*[15]	Towing tank	8.6×10^5–2.9×10^6
2021	Liu *et al.*[16]	Towing tank	1.2×10^7–3.5×10^7
2022	Khan *et al.*[17]	Wind tunnel	1.7×10^6

The aims of the present study are to investigate numerically the flows and forces at different Mach numbers, evaluate the formulas that are used widely for compressibility correction, and propose the compressibility correction of low-*Ma* flows in wind tunnels for underwater vehicles. The proposed formula can solve a class of the problem of converting the wind tunnel experiments and water tunnel/towing tank experiments for pressure coefficient of axisymmetric body of revolution.

The effects of compressibility have long been investigated in aeronautics and astronautics. Papamoschou and Roshko[19] conducted an

08 April 2024 03:18:05

Published under an exclusive license by AIP Publishing

experiment focused on the effect of compressibility on a planar shear layer, and they defined the convective Mach number as a unifying parameter for the compression effect, thereby initiating the study of compressibility effects in free shear flows. Sarkar and co-workers[20–22] used direct numerical simulations (DNS) to study the effects of compressibility in uniform shear flow, and they reported that compressibility reduces both turbulence and the energy growth rate and plays a stabilizing role. Similarly, using particle image velocimetry experiments, Beresh *et al.*[23] investigated the effects of compressibility on flow in a rectangular cavity with variable width, and they compared that case with the case of a free shear layer; the results showed that increasing *Ma* led to decreased turbulent intensity in the flows in the narrow cavities, whereas the free shear layer showed a significant decrease in the vertical direction under the influence of compressibility. There have been many outstanding studies of turbulence in incompressible flows.[24–26] Regarding compressible flows, Dong and He[27] developed an eddy-damped quasi-normal Markovian model for weakly compressible turbulence, which suggested a possible scaling in compressible energy spectra. Wang *et al.*[28] reported the effect of compressibility on small-scale structures in isotropic turbulent flows at an incoming *Ma* of approximately 1.0. The preferred eigenvalues of the strain rate tensor in the highly compressible state were found to converge to −1:0:0, which is numerically inconsistent with the case for incompressible flow, leading to a series of studies on compressible turbulence based on this inconsistency.[29–31] More recently, Jiang *et al.*[32] studied the compressibility effect of the interaction between the shock wave and turbulent boundary layer. Nilsson *et al.*[33] investigated the effects of fluid viscosity and density on the M6 wing at different *Ma*. Yu and Xu[34] investigated the compressibility effects on hypersonic wall-bounded turbulence and found the decreasing wall temperature will lead to an increase in the compressibility effect. Yang *et al.*[35] found that both the friction coefficient and the total pressure loss are affected by compressibility effect in supersonic corner flow. Karantonis *et al.*[36] revealed the flow physics of compressibility effect on suddenly expanded subsonic flows.

The effects of compressibility on subsonic flows have been investigated in detail by means of numerical simulations. Moore and Pullin[37,38] investigated numerically the propagation of vortex pairs in compressible flow, whereas most previous studies of vortex pairs involved incompressible flow.[39–41] In subsequent studies, the effects of compressibility on (i) propagation of Hill's spherical vortex[42] and (ii) a Stuart vortex array[43] were investigated, and numerical solutions were given for the steady propagation of vortices in a compressible ideal gas. Based on those results, Heister *et al.*[44] extended the numerical solutions of Moore and Pullin[42] to compressible flows with higher *Ma* (= 0.3). Sandham[45] investigated numerically the effect of compressibility on vortex pairing, showing the trend in vortex pairing caused by *Ma*. Recently, Crowdy and Krishnamurthy[46] gave analytical expressions for Karman point vortex streets in weakly compressible flow of an isentropic fluid, and they inferred that the effect of compressibility on the global equilibrium characteristics of a given vortex is a function of the geometry. Lin *et al.*[47] investigated numerically the passive scalar mixing induced by a compressible vortex ring, reporting an increased rate of entrainment due to increasing compressibility. Feng *et al.*[48] solved the 2D dimensionless compressible Navier–Stokes equations numerically to investigate sound propagation in free vortical flows.

Compressibility effects in subsonic flows have been studied in the fields of vortex dynamics and aerodynamics. Guo *et al.*[49] found that weak compressibility affects the accuracy of existing unsteady aerodynamic models; they proposed a compressibility correction model for unsteady aerodynamic force based on the variation of fluid density, which eventually reduced the error between calculation and model to approximately 5%. For ground-effect vehicles in subsonic flows, Rozhdestvensky[50] reported that compressibility effects are more significant than ground effects. Mukohara and Anyoji[51] investigated the effects of compressibility on a laminar separation bubble and the aerodynamic properties of a thick flat plate in low-*Re* subsonic flow; the results showed that compressibility helped to maintain the stability of the separated shear layer and delay the transition from laminar to turbulent flow. Teymourtash and Salimipour[52] performed numerical simulations to investigate the effect of compressibility on laminar flow past a rotating cylinder; the results showed that compressibility could influence the flow field even at low *Ma*, and with increasing *Ma*, the flow pattern was found to change from steady to one-sided vortex shedding. Wood[53] showed that compressibility degrades the performance of wind turbines, with smaller wind turbines being more affected by compressibility because of their higher blade tip speed ratios. Canuto and Taira[54] investigated 2D cylindrical winding flow in subsonic compressible flow and found that compressibility elongated the shedding wake; they emphasized that this phenomenon becomes more pronounced as *Re* approaches the critical value for shedding. Colonius *et al.*[55] studied the effect of compressibility on viscous thermally conductive vortices in unsteady flows and analyzed the mechanism for the effect of compressibility in the flow field. The results showed that compressibility generated radial velocity in the vortices, with the radial velocity in a compressible axisymmetric vortex being negative far from its core. All the aforementioned studies showed that compressibility can affect aerodynamics significantly even at relatively low *Ma*.

Different compressibility correction formulas have been proposed for the lift coefficient of airfoils, with one of the best known ones being the Prandtl–Glauert rule.[56,57] This formula establishes the relationship between the pressure coefficient in compressible flow and that in incompressible flow, with the small-perturbation assumption used to linearize the velocity potential equation for 2D inviscid subsonic uniform incoming flow. Based on the Prandtl–Glauert rule, Laitone[58] obtained a new formula containing the specific heat ratio by replacing the freestream flow *Ma* with the local *Ma*. Tsien and Kármán[59,60] developed the Karman–Tsien rule by changing the tangent point of the curve in the Chaplygin approximation; the formal difference between the Karman–Tsien rule and the Prandtl–Glauert rule is the nonlinear term in the Karman–Tsien rule. Of these three rules, the Karman–Tsien rule gives the best results for high-*Ma* flows.

Compressibility corrections have been used widely in different scenarios. Nagata *et al.*[61] used the Prandtl–Glauert rule to correct the drag coefficient of a circular cylinder in compressible low-*Re* flow. Yan and Archer[62] corrected the lift and drag coefficients of wind-turbine blades by using the Prandtl–Glauert rule. Balin *et al.*[63] used the Prandtl–Glauert transformation to recover the Helmholtz equation, which was applied in calculating the acoustic propagation of noise generated by a turbine reactor. Using computational fluid dynamics (CFD), Kirkman and Takahashi[64] investigated the geometric stretching of compressibility corrections methods. It was shown that this geometric stretching is not accurate in transforming the pressure coefficient for transonic compressible flow; rather, it should be

08 April 2024 03:18:05

Published under an exclusive license by AIP Publishing

approximated by the velocity scaling associated with *Ma*. Kontogiannis and Laurendeau[65] adopted the Prandtl–Glauert rule to improve the nonlinear vortex-lattice method, whose results agree well with the numerical simulation. Based on the Karman–Tsien rule, Xu *et al.*[66] proposed an improved 2.75D method to figure out the insufficient transformation accuracy of classical 2.75D method in subsonic flow regions. Su *et al.*[67] employed the Prandtl–Glauert rule corrected the inviscid vortex lattice method, and emphasized the effect of compressibility on flight stability. Werter *et al.*[68] promoted the continuous-time formulation to compressible flows with applying the Prandtl–Glauert transformation. Over the years, compressibility corrections have been used widely in pressure-coefficient correction for 3D shapes in different scenarios, with the Prandtl–Glauert rule, the Karman–Tsien rule, and the Laitone rule being the ones used most widely. However, the validity of these correction formulas for underwater vehicle models has not been investigated to date.

Herein, flow over an underwater vehicle model is used to investigate how compressibility affects the pressure coefficient. The underwater vehicle model is the SUBOFF model without appendages, and we solve the Navier–Stokes equations for compressible flow numerically at different *Ma*. We evaluate the performances of different formulas for compressibility correction, and we propose a new formula for correcting the SUBOFF pressure coefficient.

The rest of this paper is as follows. The numerical methods used for simulating flow around an underwater vehicle are described in Sec. II. The Prandtl–Glauert rule and the improved formulas are given in Sec. III. The results of compressibility correction with different formulas are discussed in Sec. IV. Finally, conclusions are drawn in Sec. V.

II. METHODOLOGY AND COMPUTATIONAL SETUP

A. Geometry

As the underwater vehicle model, the SUBOFF model without appendages[69] (hereinafter referred to simply as SUBOFF) is adopted in this study, as shown in Fig. 1. According to its geometry, SUBOFF can be divided into forebody, parallel middle body, and stern. The maximum diameter of SUBOFF is D, and its overall length is $L = 8.575D$. The coordinate origin (O) of the numerical simulation is set at the front of the forebody, and the Cartesian coordinate system OXYZ is used. The OX axis is parallel to the hull in the freestream direction, the OZ axis is in the spanwise direction, and the OY axis is into the page according to the right-hand rule. The angle of attack and the yaw angle are both 0° in all cases. The freestream Mach number $\mathrm{Ma} = V_\infty/c$ varies from 0.004 to 0.5, where V_∞ is the freestream velocity and c is the sound speed. The Reynolds number $\mathrm{Re}_L = V_\infty \mathrm{L}/\nu$ based on the freestream velocity V_∞ and the length L is fixed at 1.2×10^6.

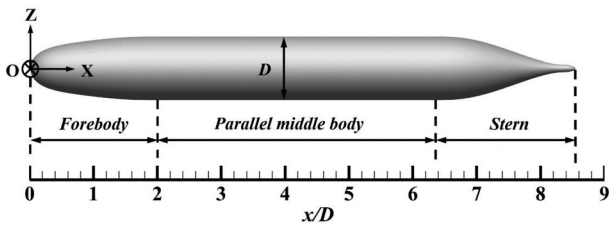

FIG. 1. Geometry of SUBOFF model without appendages.

B. Governing equations

To simulate the flow around SUBOFF, we solve the 3D compressible Reynolds-averaged Navier–Stokes (RANS) equations numerically, with the governing equations being as follows:[70]

Continuity equation

$$\frac{\partial \rho}{\partial t} + \frac{\partial}{\partial x_i}(\rho u_i) = 0. \tag{1}$$

Momentum equation

$$\frac{\partial (\rho u_i)}{\partial t} + \frac{\partial}{\partial x_j}(\rho u_i u_j) = -\frac{\partial p}{\partial x_i} + \frac{\partial}{\partial x_j}\left(\tau_{ij} + \tau_{ij}^t\right). \tag{2}$$

Energy equation

$$\frac{\partial (\rho E)}{\partial t} + \frac{\partial}{\partial x_j}(\rho H u_j) = \frac{\partial}{\partial x_j}\left[u_i\left(\tau_{ij} + \tau_{ij}^t\right) + (\mu + \sigma_k \mu_t)\frac{\partial k}{\partial x_j} + \left(\frac{c_p \mu}{Pr_l} + \frac{c_p \mu_t}{Pr_t}\right)\frac{\partial T}{\partial x_j}\right]. \tag{3}$$

In Eqs. (1)–(3), ρ, t, u_i, and x_i are pressure, time, velocity, and Cartesian coordinate, respectively. The total energy E and the total enthalpy H are given by $E = e + u_i u_i/2$ and $H = E + p/\rho$ (where e represents internal energy and p is pressure), Pr_l represents the laminar Prandtl number, Pr_t is the turbulent Prandtl number, T denotes temperature, k is turbulent kinetic energy, μ represents molecular viscosity, μ_t is turbulent eddy viscosity, σ_k is the turbulence-model constant, and c_p is the specific heat coefficient at constant pressure. The molecular stress tensor and Reynolds stress tensor are given, respectively, by

$$\tau_{ij} = \mu\left(\frac{\partial u_i}{\partial x_j} + \frac{\partial u_j}{\partial x_i}\right) - \frac{2}{3}\mu \frac{\partial u_k}{\partial x_k}\delta_{ij}, \tag{4}$$

$$\tau_{ij}^t = \mu_t\left(\frac{\partial u_i}{\partial x_j} + \frac{\partial u_j}{\partial x_i}\right) - \frac{2}{3}\mu_t \frac{\partial u_k}{\partial x_k}\delta_{ij} - \frac{2}{3}\rho k \delta_{ij}, \tag{5}$$

where δ_{ij} is the Kronecker delta.

C. Turbulence model

The two-equation shear stress transport (SST) turbulence model[71] is used to simulate the SUBOFF flow field. The SST turbulence model is a hybrid method that uses the $k-\varepsilon$ model far from the wall and the Wilcox $k-\omega$ model in the near-wall region. By combining the advantages of the Wilcox $k-\omega$ model and the transformed $k-\varepsilon$ model, relatively accurate pressure and velocity distributions can be obtained. In the SST model, the transport equations for turbulent kinetic energy (k) and specific dissipation rate (ω) are

$$\frac{\partial (\rho k)}{\partial t} + \frac{\partial (\rho u_j k)}{\partial x_j} = P - \beta^* \rho \omega k + \frac{\partial}{\partial x_j}\left[(\mu + \sigma_k \mu_t)\frac{\partial k}{\partial x_j}\right], \tag{6}$$

$$\frac{\partial (\rho \omega)}{\partial t} + \frac{\partial (\rho u_j \omega)}{\partial x_j} = \frac{\gamma}{\nu_t} P - \beta \rho \omega^2 + \frac{\partial}{\partial x_j}\left[(\mu + \sigma_\omega \mu_t)\frac{\partial \omega}{\partial x_j}\right] + 2(1 - F_1)\frac{\rho \sigma_{\omega 2}}{\omega}\frac{\partial k}{\partial x_j}\frac{\partial \omega}{\partial x_j}, \tag{7}$$

08 April 2024 03:18:05

Published under an exclusive license by AIP Publishing

where μ is molecular viscosity. The production term P is given by

$$P = \tau_{ij}^{t} \frac{\partial u_i}{\partial x_j}, \tag{8}$$

and the eddy viscosity (μ_t) is calculated as

$$\mu_t = \frac{a_1 \rho k}{\max(a_1 \omega, F_2 \Omega)}, \tag{9}$$

$$\Omega = \sqrt{2 W_{ij} W_{ij}}, \tag{10}$$

$$W_{ij} = \frac{1}{2}\left(\frac{\partial u_i}{\partial x_j} - \frac{\partial u_j}{\partial x_i}\right), \tag{11}$$

where Ω is the vorticity magnitude, W_{ij} is the rate-of-rotation tensor, and a_1 is a constant set as 0.31. The constants $\sigma_k, \beta, \sigma_\omega$ are calculated by

$$\varphi = F_1 \varphi_1 + (1 - F_1)\varphi_2, \quad (\varphi = \beta, \sigma_k, \sigma_\omega, \gamma), \tag{12}$$

$$F_1 = \tanh\left(\Gamma_1^4\right), \tag{13}$$

$$F_2 = \tanh\left(\Gamma_2^2\right), \tag{14}$$

$$\Gamma_1 = \min\left[\max\left(\frac{500\mu}{\rho\omega d^2}, \frac{\sqrt{k}}{\beta^* \omega d}\right), \frac{4\rho\sigma_{\omega 2} k}{CD_{k\omega} d^2}\right], \tag{15}$$

$$CD_{k\omega} = \max\left(2\frac{\rho\sigma_{\omega 2}}{\omega}\frac{\partial k}{\partial x_j}\frac{\partial \omega}{\partial x_j}, 1 \times 10^{-20}\right), \tag{16}$$

$$\Gamma_2 = \max\left(\frac{2\sqrt{k}}{\beta^* \omega d}, \frac{500\mu}{\rho\omega d^2}\right), \tag{17}$$

where d is the shortest distance to the wall; φ_1 and φ_2 are the parameters of the Wilcox $k-\omega$ model and the transformed $k-\varepsilon$ model, respectively; and γ is a model constant obtained as

$$\gamma_1 = \beta_1/\beta^* - \sigma_{\omega 1} k^2/\sqrt{\beta^*}, \tag{18}$$

$$\gamma_2 = \beta_2/\beta^* - \sigma_{\omega 2} k^2/\sqrt{\beta^*}. \tag{19}$$

The two aforementioned sets of coefficients are set as

$$\sigma_{k1} = 0.85, \quad \sigma_{\omega 1} = 0.5, \quad \beta_1 = 0.075, \quad C_{\omega 1} = 0.5332, \quad \beta^* = 0.09, \tag{20}$$

$$\sigma_{k2} = 1.0, \quad \sigma_{\omega 2} = 0.856, \quad \beta_2 = 0.0828, \quad C_{\omega 2} = 0.4403. \tag{21}$$

D. Numerical methods

The unstructured mesh-based cell-centered finite volume method is used in the numerical simulations, with an in-house CFD solver[72–74] used to solve the governing equations. The second-order Roe discretization scheme is employed to compute the inviscid flux, and the reconstructed scheme is adopted to obtain the viscous flux. To ensure robustness and convergence efficiency, the discretized equations are solved by the implicit lower–upper symmetric Gauss–Seidel (LU-SGS) relaxation-based implicit backward-Euler scheme.[75]

The numerical simulations are performed with a half model for the time-averaged flow field, this being because the angle of attack and yaw angle are set as 0°. The computational domain is set as a cube surrounding SUBOFF, with the XZ plane shown schematically in Fig. 2. The hull surface is set as a no-slip adiabatic boundary, and the rest of the external boundary is set as far-field and nonreflecting. The grid boundary is set to be 150D from the hull surface. A structured grid with an O–H topology is generated for the simulations, where the normal growth rate is approximately 1.15 and the first off-wall grid points are located at $y^+ \approx 1$. The total number of grid points used in the simulations is approximately 6.2×10^6. According to the work of Posa and Balaras,[76] the grid is refined near the stern, as shown in Fig. 3. The pressure coefficient and the skin friction coefficient are defined, respectively, as

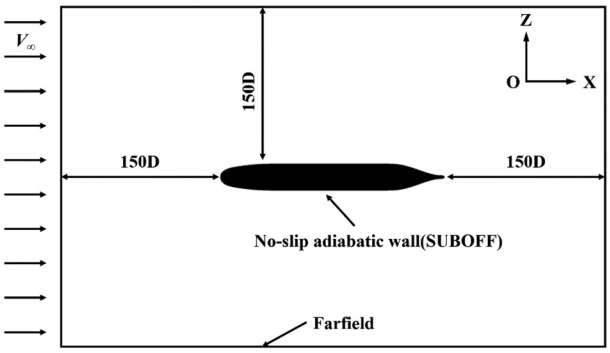

FIG. 2. Schematic of computational domain and boundary conditions.

$$C_p = \frac{p - p_\infty}{0.5\rho_\infty V_\infty^2}, \tag{22}$$

$$C_f = \frac{\tau_w}{0.5\rho_\infty V_\infty^2}, \tag{23}$$

where p_∞ is the freestream pressure, ρ_∞ is the freestream density, and p and τ_w are pressure and wall shear stress, respectively.

III. COMPRESSIBILITY CORRECTIONS

A. Prandtl–Glauert rule

As one of the best known compressibility corrections in subsonic compressible flow, the Prandtl–Glauert rule is based on the linearized perturbation velocity potential equation.[77] By transforming the governing equation of compressible flow into Laplace's equation, the relationship between compressible and incompressible flow is established. The Prandtl–Glauert rule[56,57] can be written as

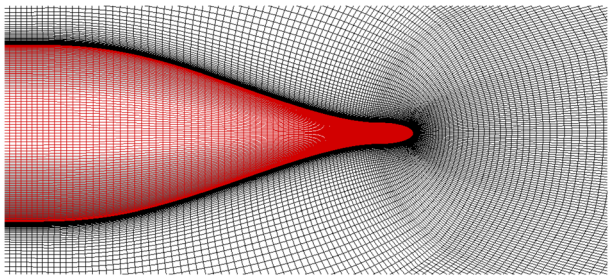

FIG. 3. Schematic of grid refinement in stern and wake regions.

08 April 2024 03:18:05

Published under an exclusive license by AIP Publishing

$$C_p = \frac{C_{p,0}}{\sqrt{1-Ma^2}}, \tag{24}$$

where C_p and $C_{p,0}$ are the pressure coefficients in compressible and incompressible flow, respectively. The compressibility correction discussed herein is the conversion of the pressure coefficient from compressible flow to incompressible flow. We rearrange Eq. (24) as

$$C_{p,0} = C_p\sqrt{1-Ma^2}. \tag{25}$$

Note that the Prandtl–Glauert rule is derived from a 2D potential and so is not exactly rigorous for correcting a 3D geometry of revolution such as SUBOFF. We consider SUBOFF as a special finite wing with a very low aspect ratio to improve the Prandtl–Glauert rule.

B. Finite-wing-analogy formula for pressure coefficient of underwater vehicles

For compressibility correction of the pressure coefficient of underwater vehicles, we propose the improved formula

$$C_{p,0} = C_p\sqrt{1-Ma^2}\frac{\zeta}{(1-2C_p\varepsilon)^{\kappa}}, \tag{26}$$

where ε and κ stand for parameters inspired by the finite-wing analogy, and ζ is a parameter that reflects the influences of SUBOFF geometry and distribution of pressure coefficient. Compared with the Prandtl–Glauert rule [Eq. (25)], the improved formula has a scale factor $\zeta/(1-2C_p\varepsilon)^{\kappa}$ on its right-hand side. We refer to Eq. (26) as the finite-wing-analogy formula because the form of this scale factor is inspired by the lift slope for a finite wing in compressible flow. The details of the analogy are as follows.

When the freestream changes from incompressible to compressible, the lift slope can be corrected as follows according to the Prandtl–Glauert transformation:

$$a_{0,\mathrm{comp}} = \frac{a_0}{\sqrt{1-Ma^2}}, \tag{27}$$

where $a_{0,comp}$ is the lift slope of an infinite wing in subsonic compressible flow, and a_0 is that for incompressible flow.

One of the models that are used most widely to predict the lift slope of a finite wing from that of an airfoil (infinite wing) is[77]

$$a_{\mathrm{comp}} = \frac{a_{0,\,\mathrm{comp}}}{\sqrt{1+\left(a_{0,\,\mathrm{comp}}/\pi AR\right)^2}+a_{0,\,\mathrm{comp}}/(\pi AR)}, \tag{28}$$

where a_{comp} is the lift slope of a finite wing in compressible flow, and AR is the aspect ratio of the finite wing. Substituting Eq. (27) into Eq. (28), the lift-slope compressibility correction formula based on an infinite wing in incompressible flow is obtained as

$$a_{\mathrm{comp}} = \frac{a_0}{\sqrt{1-Ma^2+\left[a_0/(\pi AR)\right]^2}+a_0/(\pi AR)}. \tag{29}$$

According to Eq. (29), the compressibility correction of a finite wing does not change the sign of the angle of attack, so the solution of Eq. (29) with a positive value of a_{comp} corresponding to a negative value of a_0 can be excluded. By rearranging the equation so that the pressure coefficient in incompressible flow is on the left-hand side, Eq. (29) can be re-written as

$$a_0 = a_{\mathrm{comp}}\sqrt{1-Ma^2}\frac{1}{\sqrt{1-2\vartheta_1 a_{\mathrm{comp}}}}, \tag{30}$$

where $\vartheta_1 = 1/(\pi\,\mathrm{AR})$ is a parameter that scales inversely with the aspect ratio. Note that Eq. (30) can be used when the lift slope of a finite wing in compressible flow falls within the scope of $a_{comp} < \pi AR/2$.

Inspired by the form of Eq. (30), we propose a formula for transforming the pressure coefficient from compressible flow (C_p) to incompressible flow ($C_{p,0}$) as

$$C_{p,0} = C_p\sqrt{1-Ma^2}\frac{\zeta_1}{\sqrt{1-2\varepsilon_1 C_p}}, \tag{31}$$

where ζ_1 and ε_1 are parameters related to the finite-wing analogy. Corresponding to Eq. (30), the physical meaning of the term $\sqrt{1-Ma^2}$ is the compressibility correction, $\sqrt{1-2\varepsilon_1 C_p}$ is the finite-wing-analogy correction, and ζ_1 is the correction from 2D to 3D for SUBOFF. Equation (31) is a specific form of Eq. (26) with $\kappa = 1/2$, $\zeta = \zeta_1$, and $\varepsilon = \varepsilon_1$.

Another widely used model for predicting the lift slope of a finite wing from that of an airfoil (infinite wing) is[77]

$$a_0 = a_{\mathrm{comp}}\sqrt{1-Ma^2}\frac{1}{1-2\vartheta_2 a_{\mathrm{comp}}}, \tag{32}$$

where $\vartheta_2 = 1/(2\pi\,\mathrm{AR})$ is again a parameter that scales inversely with the aspect ratio. Inspired by the form of Eq. (32), we propose another formula for transforming the pressure coefficient of compressible flow (C_p) to incompressible flow ($C_{p,0}$) as

$$C_{p,0} = C_p\sqrt{1-Ma^2}\frac{\zeta_2}{1-2\varepsilon_2 C_p}, \tag{33}$$

where ζ_2 and ε_2 are parameters related to the finite-wing analogy. Equation (33) is a specific form of Eq. (26) with $\kappa = 1$, $\zeta = \zeta_2$, and $\varepsilon = \varepsilon_2$.

Hereinafter, we refer to the correction formulas given by Eqs. (31) and (33) as correction formula I (CF-I) and correction formula II (CF-II), respectively. The values of the correction factors ζ_1, ζ_2 and the aspect-ratio analogy factors ε_1, ε_2 are given in Sec. IV based on the pressure-coefficient distribution of SUBOFF.

IV. RESULTS AND DISCUSSION

A. Overview of flow

The time-averaged fields of axial velocity, pressure coefficient, and vortex magnitude at $Ma = 0.03$ in the XZ plane are shown in Fig. 4. Most of the flow field has a negative pressure coefficient, but it is positive near the forehead and stern, as shown in Fig. 4(b). Here, the pressure coefficient is defined by Eq. (22). The pressure decreases rapidly after the stagnation point and then increases slowly before the parallel middle body, but it remains lower than the freestream pressure. On the parallel middle body, the pressure changes slowly, decreasing to a high negative pressure coefficient again at the end of the parallel middle body. Then, the flow convergence at the stern generates high pressure, but the peak pressure is lower than that of the stagnation

08 April 2024 03:18:05

Published under an exclusive license by AIP Publishing

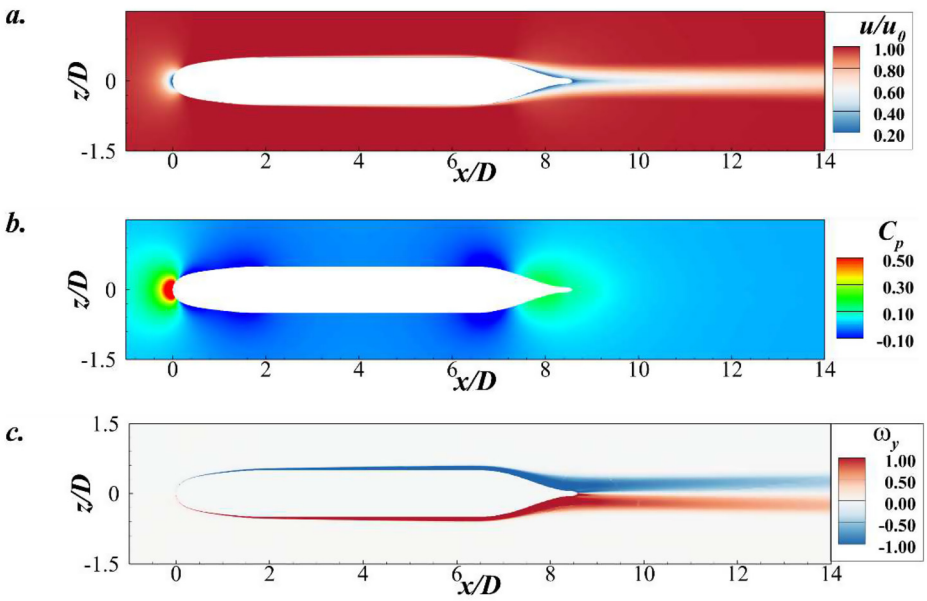

FIG. 4. Time-averaged fields in XZ plane: (a) axial velocity; (b) pressure coefficient; and (c) vorticity magnitude.

point. The thickness of the boundary layer increases gradually along the hull, as shown in Fig. 4(c).

The distributions of time-averaged pressure coefficient and skin-friction coefficient for $Ma = 0.03$ are plotted in Fig. 5, where also plotted are the experimental results of Huang *et al.*[2] and Liu *et al.*[4] and the numerical simulation results of Liu *et al.*[74] based on detached eddy simulation (DES). Of these results, the estimated experimental error of C_p of Liu *et al.*[4] is about 0.05. As can be seen from Fig. 5(a), the predicted pressure coefficient agrees well with the experimental and numerical results. The average error between the predicted results and the experimental results of Liu *et al.*[4] is 0.63%. For the skin-friction coefficient, the predicted results agree well with both the experimental and DES ones, with the average error between the RANS and DES results being 3.6%.

B. Correction of pressure coefficient

The distributions of the pressure coefficient are shown in Fig. 6, in which there are four positive peaks and three negative peaks. The first positive peak is at the stagnation point, after which the pressure coefficient drops rapidly to negative values, and the first negative peak is in the front of the forebody. After that, the pressure coefficient increases and then decreases, forming the second positive peak and the second negative peak, respectively. The pressure coefficient at the parallel middle body changes slowly, maintaining a trend of increasing and then decreasing. The third positive peak is located at approximately the midpoint of the hull. At the end of the parallel middle body, the pressure coefficient decreases and forms the third negative peak, which is also the minimum value of the pressure coefficient.

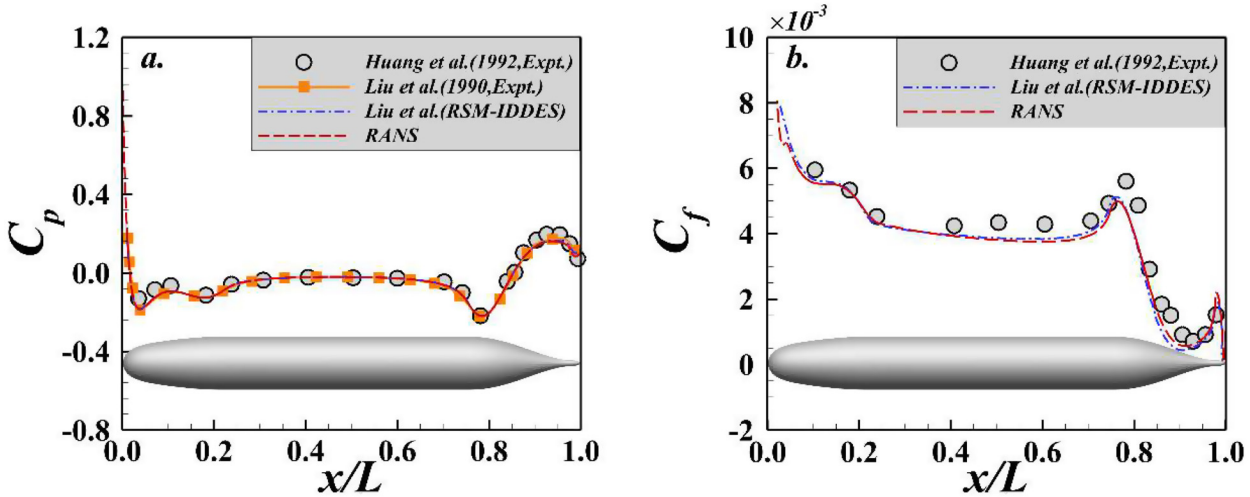

FIG. 5. Time-averaged distributions of (a) pressure coefficient C_p and (b) skin-friction coefficient C_f for $Ma = 0.03$.

08 April 2024 03:18:05

Published under an exclusive license by AIP Publishing

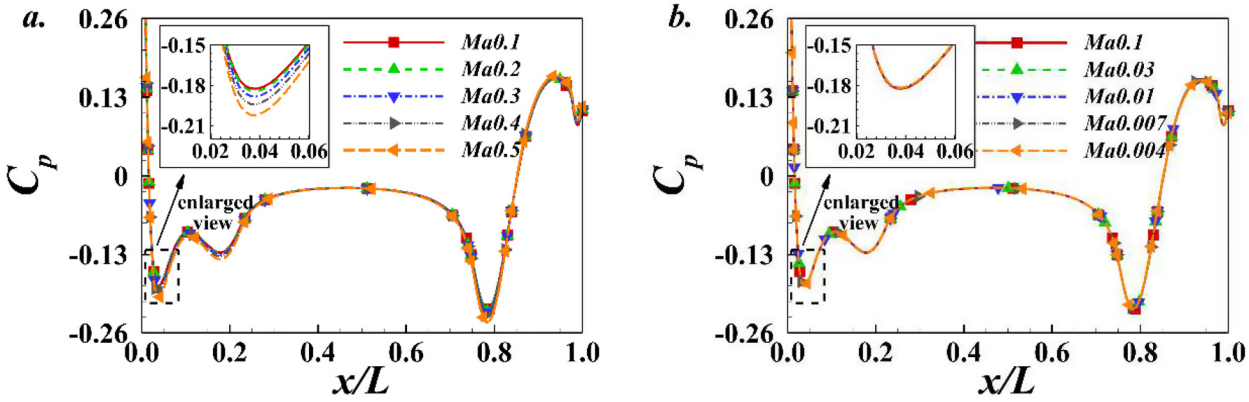

FIG. 6. Distribution of pressure coefficient on hull at different Mach numbers: (a) $Ma \geq 0.1$ and (b) $Ma \leq 0.1$.

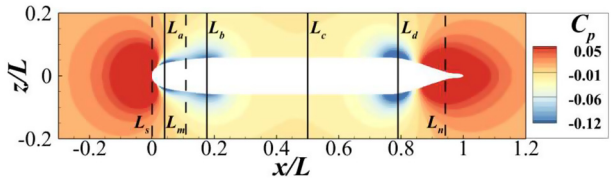

FIG. 7. Pressure distribution in near-wall region in XZ plane. Solid lines—(L_a, L_b, L_c, L_d) corresponding to the locations (a, b, c, d) of the pressure-coefficient peaks; dashed lines—(L_s, L_m, L_n) corresponding to the locations (s, m, n) of the pressure-coefficient peaks.

The pressure coefficient increases in the stern region and reaches the fourth positive peak near the end of the hull. In summary, the curve of the SUBOFF pressure coefficient has a total of seven peaks, three negative ones and four positive ones; the negative peaks are located at $x/L = 0.04$, 0.18, and 0.78, and the positive peaks are located at $x/L = 0.0$, 0.11, 0.5, and 0.94. The corresponding locations of the pressure-coefficient peaks on the hull are shown in Fig. 7 by solid lines (L_a, L_b, L_c, L_d) and dashed lines (L_s, L_m, L_n), respectively.

The pressure coefficient at different Mach numbers for $Ma \geq 0.1$ is compared in Fig. 6(a). As can be seen, the negative peaks of the pressure coefficient decrease with increasing Ma, and the difference in the pressure coefficient between two adjacent values of Ma increases with Ma. Comparing Figs. 6(a) and 6(b) shows that the pressure coefficient at different values of Ma at the locations of the pressure-coefficient peaks differs significantly for $Ma \geq 0.1$, whereas this difference is negligible for $Ma \leq 0.1$. The values of the pressure coefficient at six of the peaks are given in Table II; because the pressure coefficient at the stagnation point is $C_{p,x/L=0.0} = 1$, we do not consider its correction there. According to Table II, for $Ma \geq 0.1$, the sum of the absolute values of the maximum difference of the pressure coefficient for the six remaining locations is

$$\sum_{i=1}^{6} |C_{p,i,Ma=0.5} - C_{p,i,Ma=0.1}| = 6.5 \times 10^{-2}, \tag{34}$$

whereas the value for $Ma \leq 0.1$ is

$$\sum_{i=1}^{6} |C_{p,i,Ma=0.004} - C_{p,i,Ma=0.1}| = 0.4 \times 10^{-2}. \tag{35}$$

Therefore, herein we focus on evaluating the compressibility corrections for $Ma \geq 0.1$ (i.e., when the compressibility effect must be accounted for). Based on the above analysis, we use the numerical simulation results for $Ma = 0.1$ as a reference for incompressible flow in the subsequent study, as was done by Kármán.[60]

We define the maximum difference of the pressure coefficient at different locations as

TABLE II. Positive and negative peaks of pressure coefficient at different values of Mach number.

Ma	$C_{p,x/L=0.04}$	$C_{p,x/L=0.11}$	$C_{p,x/L=0.18}$	$C_{p,x/L=0.50}$	$C_{p,x/L=0.78}$	$C_{p,x/L=0.94}$
0.004	−0.182	−0.0926	−0.126	−0.0202	−0.220	0.159
0.007	−0.182	−0.0926	−0.126	−0.0202	−0.220	0.160
0.01	−0.182	−0.0926	−0.126	−0.0202	−0.220	0.160
0.03	−0.182	−0.0926	−0.126	−0.0202	−0.220	0.160
0.1	−0.182	−0.0928	−0.127	−0.0202	−0.221	0.161
0.2	−0.185	−0.0936	−0.128	−0.0203	−0.223	0.161
0.3	−0.188	−0.0948	−0.130	−0.0204	−0.227	0.162
0.4	−0.194	−0.0968	−0.133	−0.0205	−0.233	0.164
0.5	−0.202	−0.0996	−0.138	−0.0216	−0.242	0.166

08 April 2024 03:18:05

Published under an exclusive license by AIP Publishing

TABLE III. Coordinate locations of four typical locations on SUBOFF.

Typical location	Coordinate location
a	$x/L = 0.04$
b	$x/L = 0.18$
c	$x/L = 0.5$
d	$x/L = 0.78$

$$\Delta C_{p,\max} = \left| \frac{C_{p,Ma=0.5} - C_{p,Ma=0.1}}{C_{p,Ma=0.1,\min}} \right|, \tag{36}$$

where $C_{p,Ma=0.1,\min}$ is the minimum value of the pressure coefficient on the hull for $Ma = 0.1$. The maximum difference of the pressure coefficient at the first negative peak is $\Delta C_{p,\max,x/L=0.11} = 3.17\%$. The final positive peak at $x/L = 0.94$ is located in the stern region, and the maximum difference $\Delta C_{p,\max,x/L=0.94} = 2.26\%$ of the pressure coefficient indicates that here it is affected less by Ma. The maximum differences of the pressure coefficient at the other four peaks are $\Delta C_{p,\max,x/L=0.04} = 9.05\%$, $\Delta C_{p,\max,x/L=0.18} = 4.98\%$, $\Delta C_{p,\max,x/L=0.5} = 0.45\%$, and $\Delta C_{p,\max,x/L=0.78} = 9.50\%$, respectively; therefore, we select $x/L = 0.04$, $x/L = 0.18$, and $x/L = 0.78$ as typical locations for the pressure correction. Liu *et al.*[4] reported that $x/L = 0.04$ and $x/L = 0.78$ are the two most sensitive locations during pressure measurements in wind tunnel tests, which supports the present choice of the typical locations at $x/L = 0.04$ and $x/L = 0.78$. We also add $x/L = 0.5$ as another typical location in order to investigate the compressibility correction in the zone of zero pressure gradient. The four typical locations for correcting the pressure coefficient are labeled as a, b, c, and d in Fig. 7, and the corresponding coordinates are given in Table III. The subsequent correction of the pressure coefficient is done at these four typical locations, where it is negative; hence, the compressibility correction for SUBOFF is aimed mainly at the part where $C_p < 0$.

1. Prandtl–Glauert rule

First, we use the Prandtl–Glauert rule to correct the pressure coefficient of SUBOFF in compressible flow. The formula is evaluated by comparing the corrected and uncorrected compressibility errors, which are defined, respectively, as

$$\eta_{uncor} = \frac{|C_{p,Ma=0.5} - C_{p,Ma=0.1}|_{uncor}}{|C_{p,Ma=0.1,\min}|}, \tag{37}$$

$$\eta_{cor} = \frac{|C_{p,Ma=0.5} - C_{p,Ma=0.1}|_{cor}}{|C_{p,Ma=0.1,\min}|}, \tag{38}$$

where the subscript *uncor* indicates the uncorrected result and *cor* indicates the corrected one. The overall correction effect of the formula at the four typical locations listed in Table II is measured by comparing the average correction factor

$$\xi = 1 - \frac{\overline{\eta_{cor}}}{\overline{\eta_{uncor}}}, \tag{39}$$

where $\overline{\eta_{uncor}}$ is the average of the compressibility error at the four typical locations without correction, and $\overline{\eta_{cor}}$ is that of the corrected results. The variable ξ indicates the convergence of the pressure-coefficient curve at different Ma transformed by the correction formula: the uncorrected value is zero, whereas a value close to unity indicates a small difference of the pressure coefficient at different Ma (i.e., a better correction effect).

Figure 8 shows the corrected results of the Prandtl–Glauert rule for the pressure coefficient at the four typical locations. The uncorrected and corrected compressibility errors at a are $\eta_{uncor,a} = 8.85\%$ and $\eta_{cor,PG,a} = 2.98\%$, respectively, and at b ($x/L = 0.18$), they are $\eta_{uncor,b} = 5.51\%$ and $\eta_{cor,PG,b} = 2.97\%$, respectively. Although the correction effect at b is slightly worse than that at a, the corrected result is still an improvement over the uncorrected value. Typical location c ($x/L = 0.5$) is located at the middle of the hull, where the pressure coefficient changes gently, and the pressure-coefficient difference at different Ma is smaller than that at the other typical locations. The uncorrected compressibility error is $\eta_{uncor,c} = 0.20\%$, whereas the corrected value is $\eta_{cor,PG,c} = 1.00\%$. As can be seen, the corrected pressure-coefficient curve is more scattered at c, and the corrected compressibility error is larger than the uncorrected one. However, the corrected compressibility error increases to only 1%, which is still acceptable. The compressibility errors of the uncorrected and corrected result at d ($x/L = 0.78$) are $\eta_{uncor,d} = 9.48\%$ and $\eta_{cor,PG,d} = 4.69\%$, where the corrected compressibility error is roughly half the uncorrected one. The average correction factor of the Prandtl–Glauert rule is $\xi_{PG} = 0.51$, which indicates effective correction of the SUBOFF pressure coefficient.

The values of the uncorrected and corrected pressure coefficient at typical location a are given in Table IV. Figure 8 and Table IV show that the uncorrected pressure coefficient decreases with increasing Ma, whereas the corrected one increases. This difference in the trends of the uncorrected and corrected pressure coefficient with Ma reflects the overcorrection characteristic of the Prandtl–Glauert rule for the pressure coefficient of 3D geometries of revolution such as SUBOFF.

2. Karman–Tsien rule

The Karman–Tsien rule is based on the adiabatic relationship of gases, where the tangent point of the curve in the Chaplygin approximation is changed from stationary point to free flow. The relationship between compressible and incompressible flows is established based on the hodograph method, and finally, a correction quantity with a connection to the local pressure coefficient is obtained. Compared with the Prandtl–Glauert rule, the Karman–Tsien rule has a larger range of applicability for different Ma and shows a better correction effect at higher Ma for 2D airfoils. Aiming at examining the effect of the Karman–Tsien rule on the correction of the pressure coefficient of a geometry of revolution in low-speed subsonic flow, the same parameters as those used with the Prandtl–Glauert rule are selected for comparison. The Karman–Tsien rule is given as

$$C_p = \frac{C_{p,0}}{\sqrt{1 - Ma^2} + \left(\frac{Ma^2}{1 + \sqrt{1 - Ma^2}} \right) \frac{C_{p,0}}{2}}, \tag{40}$$

where the parameters have the same physical meanings as those in the Prandtl–Glauert rule. The pressure coefficient in incompressible flow is obtained as

08 April 2024 03:18:05

Published under an exclusive license by AIP Publishing

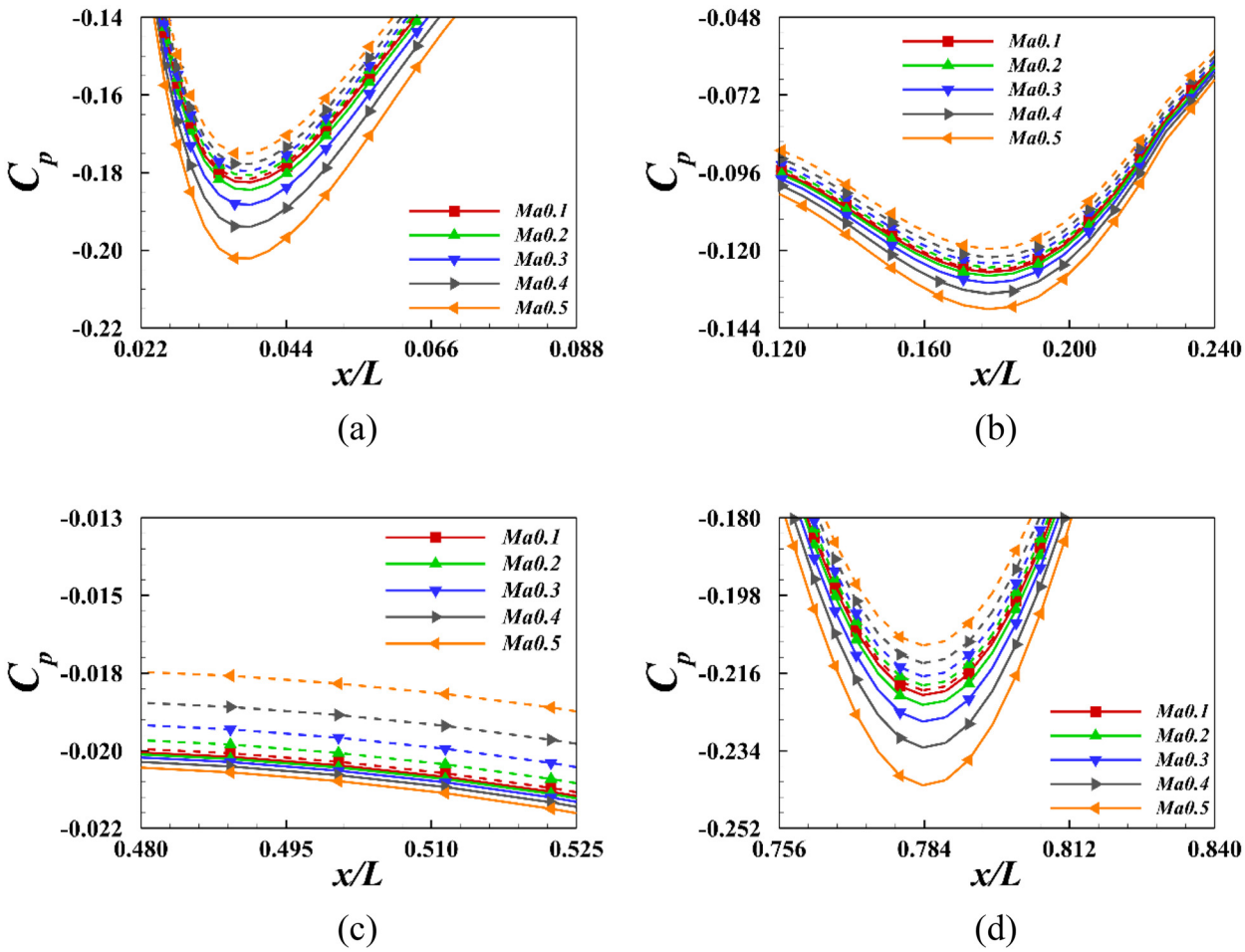

FIG. 8. Corrected results of the Prandtl–Glauert rule for pressure coefficient at typical locations of SUBOFF: (a) $x/L = 0.04$; (b) $x/L = 0.18$; (c) $x/L = 0.5$; and (d) $x/L = 0.78$. Solid lines—pressure coefficient at different *Ma* without correction; dashed lines—corrected pressure coefficient. The other correction formulas are compared in the same way.

$$C_{P,0} = \frac{C_P\sqrt{1-Ma^2}}{1-\left(\frac{Ma^2}{1+\sqrt{1-Ma^2}}\right)\frac{C_P}{2}}. \tag{41}$$

The corrected results of the Karman–Tsien rule for the pressure coefficient of SUBOFF are shown in Fig. 9. As shown in Figs. 8 and 9, there are several similarities between the corrections of the Karman–Tsien and Prandtl–Glauert rules: (i) the Karman–Tsien rule also exhibits overcorrection of the pressure coefficient of SUBOFF; (ii) the corrected compressibility errors of the Karman–Tsien rule in the zero-pressure-gradient region are larger than those of the uncorrected results. Next, the corrected results of the two formulas are compared numerically. The corrected result of the pressure coefficient at *a* with the Karman–Tsien rule is $\eta_{cor,KT,a} = 4.00\%$, which is greater than that with the Prandtl–Glauert rule ($\eta_{cor,PG,a} = 2.98\%$). At the other typical locations, the compressibility errors of the Karman–Tsien rule are $\eta_{cor,KT,b} = 3.45\%$, $\eta_{cor,KT,c} = 1.01\%$, and $\eta_{cor,KT,d} = 6.15\%$. To compare the correction effect, the compressibility errors of the Prandtl–Glauert rule are given again as $\eta_{cor,PG,b} = 2.97\%$, $\eta_{cor,PG,c} = 1.00\%$, and $\eta_{cor,PG,d} = 4.69\%$. The average correction factors of these two formulas are $\xi_{KT} = 0.38$ and $\xi_{PG} = 0.51$.

TABLE IV. Uncorrected and corrected pressure coefficient at typical location *a*.

Ma	$C_{p,uncor}$	$C_{p,cor}$
0.1	−0.182	−0.182
0.2	−0.185	−0.181
0.3	−0.188	−0.180
0.4	−0.194	−0.178
0.5	−0.202	−0.175

According to the above data, the overcorrection characteristic of the Karman–Tsien rule is more significant than that of the Prandtl–Glauert rule, which can also be seen by analyzing the forms of the two formulas. For the Prandtl–Glauert rule, when the pressure coefficient in incompressible flow is positive, the obtained pressure

08 April 2024 03:18:05

Published under an exclusive license by AIP Publishing

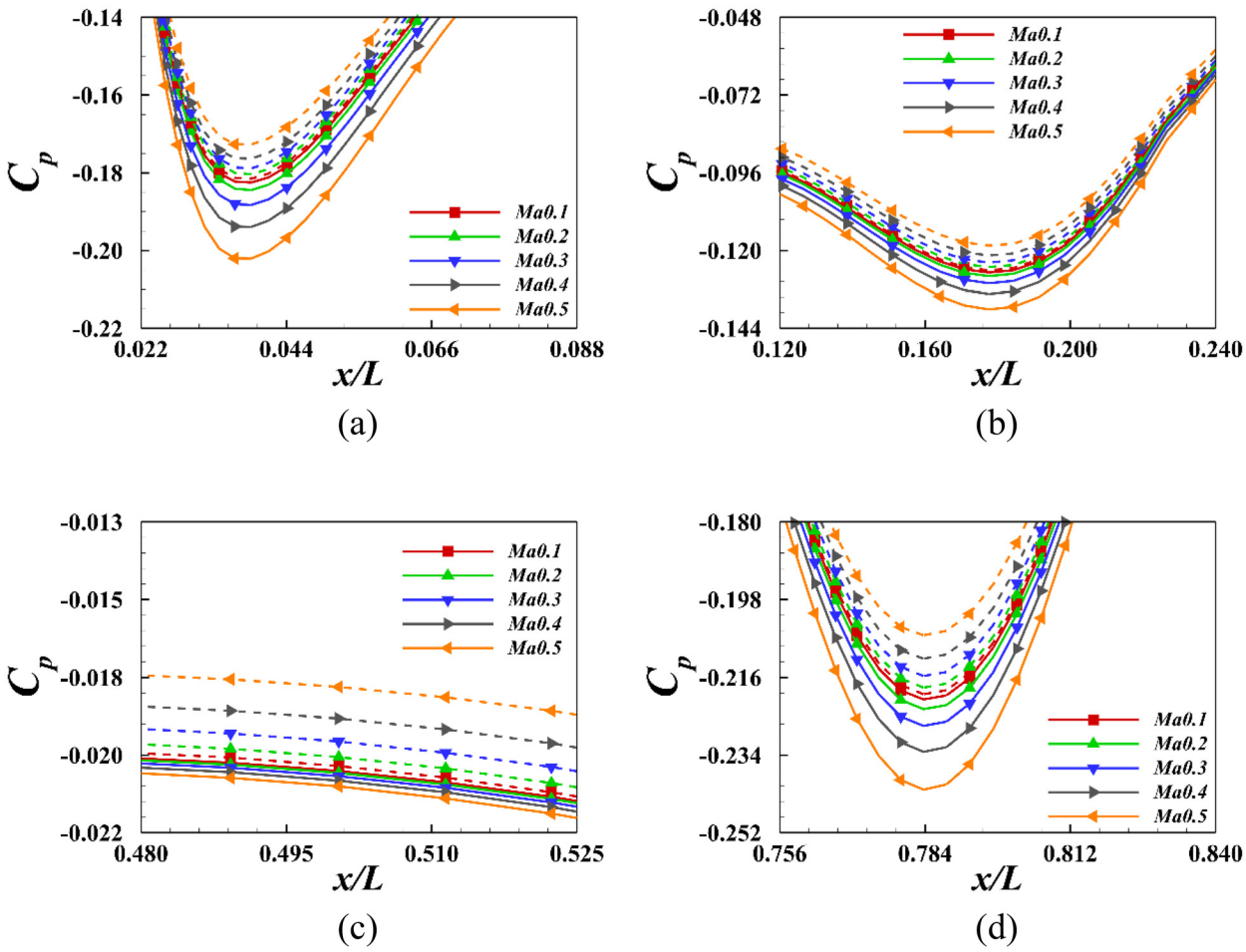

FIG. 9. Corrected results of Karman–Tsien rule for pressure coefficient at typical SUBOFF locations: (a) $x/L = 0.04$; (b) $x/L = 0.18$; (c) $x/L = 0.5$; and (d) $x/L = 0.78$.

coefficient in compressible flow is larger than that in incompressible flow, because the denominator is always smaller than unity, whereas the value in compressible flow is smaller when the pressure coefficient in incompressible flow is negative. In other words, the Prandtl–Glauert rule leads to an increased pressure coefficient when a negative pressure coefficient is transformed from compressible flow to incompressible flow. As mentioned earlier, the Karman–Tsien rule is formally based on the Prandtl–Glauert rule with a nonlinear correction term in the denominator. Because the nonlinear term contains the pressure coefficient for incompressible flow, the corrected pressure coefficient for compressible flow is smaller than that of the Prandtl–Glauert rule when the pressure coefficient is negative. In other words, the Karman–Tsien rule leads to a larger increase in the pressure coefficient when a negative one is transformed from compressible to incompressible flow. The typical locations used herein are under negative pressure, and the overcorrection characteristic of the Prandtl–Glauert rule implies an excessive increase in the pressure coefficient from compressible to incompressible flow. Therefore, a large increase in the corrected pressure coefficient leads to the Karman–Tsien rule having a significant overcorrection characteristic.

3. Laitone rule

The Laitone rule and the Karman–Tsien rule are similar in that both contain a nonlinear correction term, the difference being that the nonlinear correction term in the Laitone rule contains the specific heat ratio. When the correction effects of the three aforementioned formulas were evaluated for a NACA4412 airfoil,[78] the Laitone rule overestimated the experimental results, the Prandtl–Glauert rule underestimated them, and the Karman–Tsien rule provided the best agreement. However, the correction effects of these three formulas on the SUBOFF pressure coefficient remain to be investigated. The Laitone rule is given as

$$C_p = \frac{C_{p,0}}{\sqrt{1-Ma^2} + \frac{Ma^2}{\sqrt{1-Ma^2}}\left(1 + \frac{\gamma_G - 1}{2}Ma^2\right)\frac{C_{p,0}}{2}}, \quad (42)$$

where γ_G is the specific heat ratio of the gas. For the freestream conditions given herein, γ_G is not strictly equal to 1.4 but is very close to it. Nevertheless, being proportional to Ma^2, the term $\frac{\gamma_G - 1}{2}Ma^2$ is small compared with unity, and for the term $\frac{Ma^2}{\sqrt{1-Ma^2}}$, its numerator Ma^2 is

08 April 2024 03:18:05

Published under an exclusive license by AIP Publishing

either less than or much less than unity and so is small compared with its denominator $\sqrt{1-Ma^2}$; therefore, variations in γ_G within a small range have negligible effect on the pressure coefficient. According to the Laitone rule, the pressure coefficient for incompressible flow can be obtained as

$$C_{P,0} = \frac{C_P\sqrt{1-Ma^2}}{1-\frac{Ma^2}{\sqrt{1-Ma^2}}\left(1+\frac{\gamma_G-1}{2}Ma^2\right)\frac{C_P}{2}}. \quad (43)$$

The corrected results of the Laitone rule for the pressure coefficient at the typical locations are shown in Fig. 10. As before, the corrected results of the Laitone rule reflect its overcorrection characteristics, as shown in Fig. 10, with the compressibility errors at the typical locations after correction being $\eta_{cor,Lai,a} = 5.25\%$, $\eta_{cor,Lai,b} = 4.05\%$, $\eta_{cor,Lai,c} = 1.03\%$, and $\eta_{cor,Lai,d} = 7.94\%$. The average correction factor is $\zeta_{Lai} = 0.23$, which indicates that the Laitone rule is not as effective as the Prandtl–Glauert rule and the Karman–Tsien rule in correcting the SUBOFF pressure coefficient. There are two differences between the compressibility corrections of these three formulas for the 3D SUBOFF model and the 2D NACA4412 airfoil: (i) all three formulas overcorrect in the SUBOFF compressibility correction, which differs from the both overestimated and underestimated corrected results for the NACA4412 airfoil; (ii) for the compressibility correction of the NACA4412 airfoil, the correction effect is ordered as the Karman–Tsien rule > the Laitone rule > the Prandtl–Glauert rule, whereas for the SUBOFF pressure coefficient, it is the Prandtl–Glauert rule > the Karman–Tsien rule > the Laitone rule. Moreover, the compressibility correction formulas derived from a 2D airfoil do not perform well in correcting the SUBOFF pressure coefficient. According to the data above, the maximum average correction factor is $\xi_{PG} = 0.51$, which is still far from the optimal value of unity.

4. Finite-wing-analogy formulas

Figure 11 shows the corrected results of CF-I [Eq. (31)] for the SUBOFF pressure coefficient at the four typical locations with $\varepsilon_1 = -1.1$ and $\zeta_1 = 0.77$. At the typical locations of the negative pressure-coefficient peaks (i.e., locations *a*, *b*, and *d*), the corrected results of CF-I show good convergence. Numerically, the

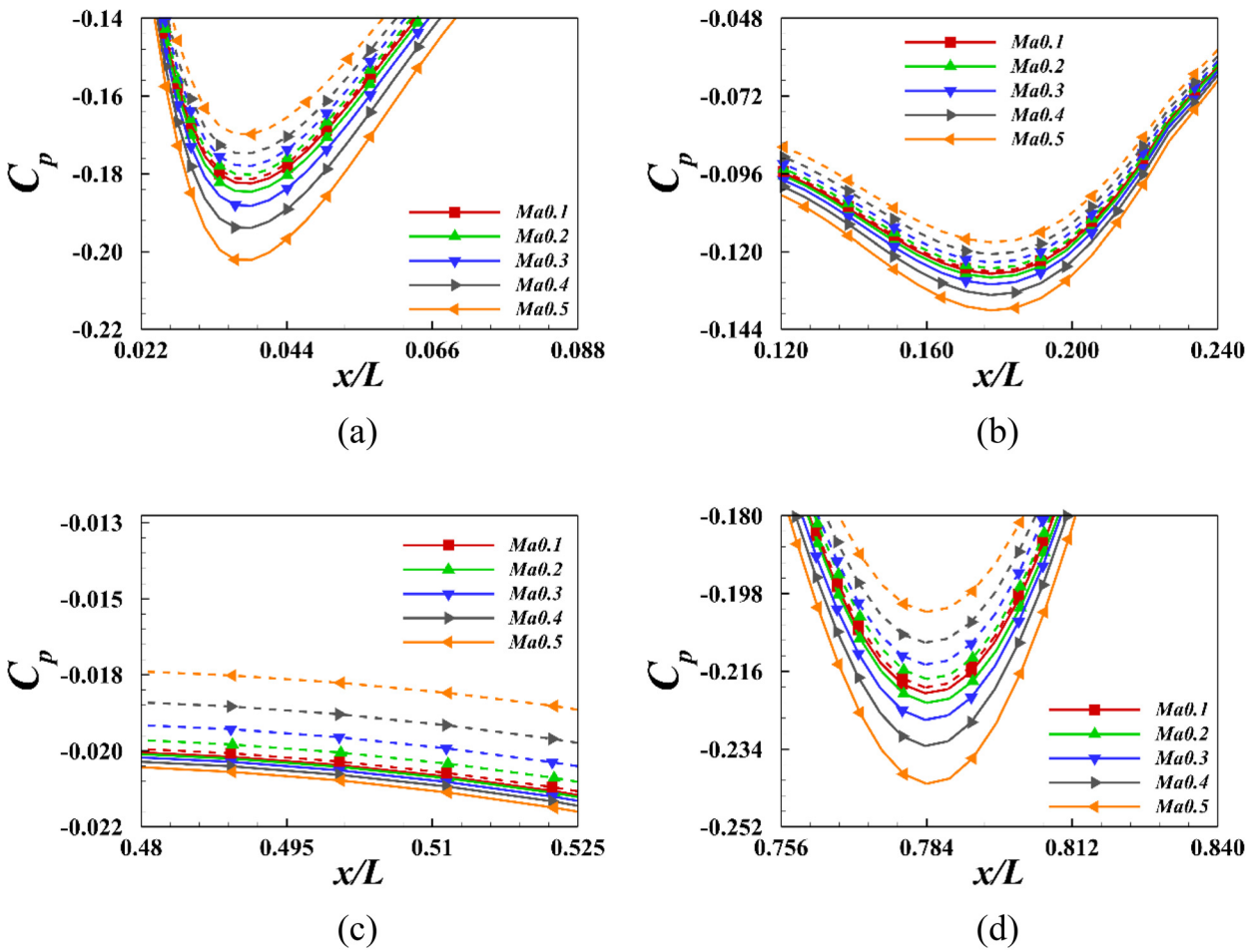

FIG. 10. Corrected results of Laitone rule for pressure coefficient at typical SUBOFF locations: (a) $x/L = 0.04$; (b) $x/L = 0.18$; (c) $x/L = 0.5$; and (d) $x/L = 0.78$.

08 April 2024 03:18:05

Published under an exclusive license by AIP Publishing

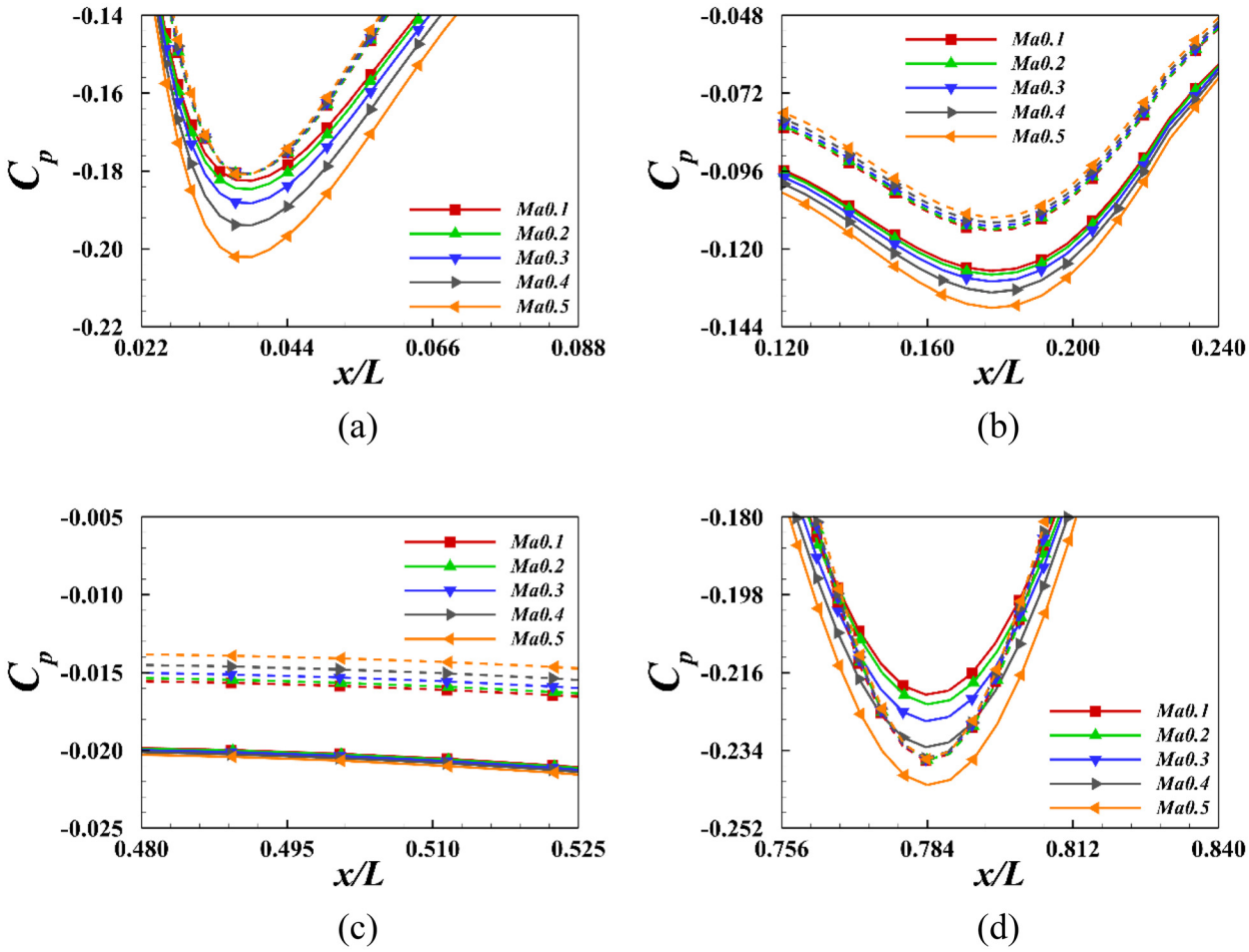

FIG. 11. Corrected results of correction formula I for SUBOFF pressure coefficient at typical locations: (a) $x/L = 0.04$; (b) $x/L = 0.18$; (c) $x/L = 0.5$; and (d) $x/L = 0.78$.

compressibility errors at each typical location after correction are $\eta_{cor,For-I,a} = 0.03\%$, $\eta_{cor,For-I,b} = 1.83\%$, $\eta_{cor,For-I,c} = 0.79\%$, and $\eta_{cor,For-I,d} = 0.14\%$, and the average correction factor of CF-I is $\xi_{For-I} = 0.88$. According to the compressibility error and the average correction factor, CF-I outperforms the Prandtl–Glauert rule, the Karman–Tsien rule, and the Laitone rule for correcting the SUBOFF pressure coefficient. At locations *a* and *d*, the results for the pressure coefficient at different *Ma* almost overlap, and at location *a*, the corrected results nearly overlap with the results for incompressible flow (i.e., $Ma = 0.1$). This means that the pressure coefficients in compressible flow can be transformed to very close values.

Although CF-I shows good convergence at the locations of the pressure-coefficient peaks, differences remain between the corrected pressure coefficient for compressible flow and the uncorrected one for incompressible flow. To correct the pressure coefficient for compressible flow to equal that for incompressible flow while also ensuring convergence, we developed CF-II [Eq. (33)] based on another finite-wing lift-slope formula. By introducing characteristic values of the SUBOFF pressure coefficient, CF-II can be improved with

$$\zeta_2 = e^{4.2\left(C_p-\overline{C_{p,0}}\right)\sqrt{\left|(x/L)-\sum_{i=1}^{4} C_{p,i}(x/L)_i/\sum_{i=1}^{4} C_{p,i}\right|}}, \tag{44}$$

where e is Euler's number, $\overline{C_{p,0}} = 0.0367$ is the average value of the SUBOFF pressure coefficient, and $\sum_{i=1}^{4} C_{p,i}(x/L)_i/\sum_{i=1}^{4} C_{p,i} = 0.386$ is the moment center of the pressure coefficient at all typical locations. CF-II can be rearranged as

$$C_{p,0} = C_p\sqrt{1-Ma^2}\,\frac{e^{4.2(C_p-0.0367)\sqrt{|(x/L)-0.386|}}}{1-2\varepsilon_2 C_p}, \tag{45}$$

where the value of the pressure coefficient correction factor is set as $\varepsilon_2 = -1.15$, and CF-II [Eq. (45)] is used for the SUBOFF pressure-coefficient correction, as shown in Fig. 12.

Comparing Figs. 11 and 12, the results of CF-II [Eq. (45)] show good convergence at each local location and agree better with the pressure coefficient for incompressible flow than is the case with CF-I. The compressibility errors of the pressure coefficient at each typical location obtained by CF-II are $\eta_{cor,For-II,a} = 0.38\%$, $\eta_{cor,For-II,b} = 2.18\%$,

08 April 2024 03:18:05

Published under an exclusive license by AIP Publishing

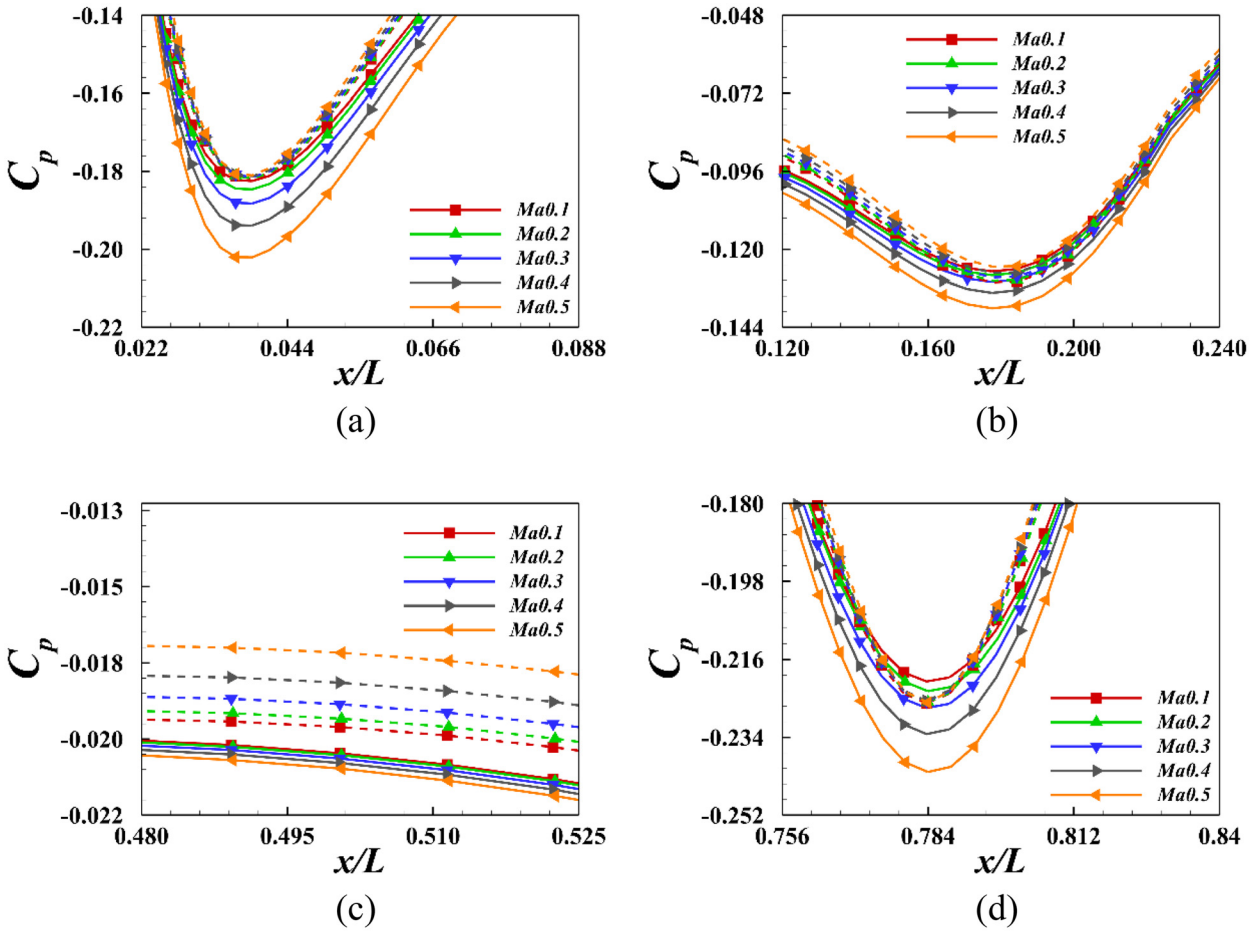

FIG. 12. Corrected results of correction formula II for SUBOFF pressure coefficient at typical locations: (a) $x/L = 0.04$; (b) $x/L = 0.18$; (c) $x/L = 0.5$; and (d) $x/L = 0.78$.

$\eta_{cor,For-II,c} = 0.97\%$, and $\eta_{cor,For-II,d} = 0.16\%$, and the average correction factor is $\xi_{For-II} = 0.84$, which is close to that of CF-I. Based on the above results, CF-II ensures convergence of the pressure coefficient at different *Ma* and corrects the pressure coefficient for compressible flow to match well with that for incompressible flow.

The above analysis shows that both CF-I and CF-II have good convergence for the SUBOFF pressure coefficient. Next, we examine the abilities of the different compressibility corrections to transform the pressure coefficient from compressible to incompressible flow. The differences in the pressure coefficient corrected by the different formulas with varying *Ma* are shown in Fig. 13. The pressure-coefficient difference ΔC_p at each typical location is calculated as

$$\Delta C_p = C_p - C_{p,Ma=0.1}, \tag{46}$$

where $C_{p,Ma=0.1}$ is the pressure coefficient for incompressible flow at the typical locations.

According to the physical meaning of the pressure-coefficient difference ΔC_p, the absolute value of the slope of the curve represents the convergence of the pressure coefficient at different *Ma*. As can be seen in Fig. 13, at typical locations *a*, *b*, and *d*, the absolute value of the slope of the corrected curve of each formula is smaller than that without correction, which verifies again that all the formulas used above have a corrective effect on the pressure coefficient. Meanwhile, at typical locations *a* and *d*, the curves obtained by the finite-wing-analogy formulas are almost parallel to the baseline. Although CF-I has the best convergence, its pressure-coefficient difference ΔC_p at typical locations *b*, *c*, and *d* is larger than those of the other formulas, indicating a poor ability of CF-I in correcting the pressure coefficient from compressible flow to incompressible flow. By contrast, CF-II has the best convergence and compressibility correction ability of all the formulas.

The SUBOFF model is considered as a very small aspect-ratio body of revolution. The proposed formula was obtained by analogizing the pressure coefficient correction formula of finite-wing. Taking Eq. (31) as example, the form of the formula is based on the Prandtl–Glauert rule with an additional correction term introduced. According to the derivation of Prandtl–Glauert rule, the pressure coefficient is related to the term $\sqrt{1 - Ma^2}$ when the thickness is constant.[79] The correction term contains variables ζ and ε, whose value can be adjusted to correct the "over-correction" characteristic of the Prandtl–Glauert rule. Similarity, the value of variables can be adjusted to correct the Prandtl–Glauert rule in the case when the Prandtl–Glauert rule is "under-correction." At the same time,

08 April 2024 03:18:05

Published under an exclusive license by AIP Publishing

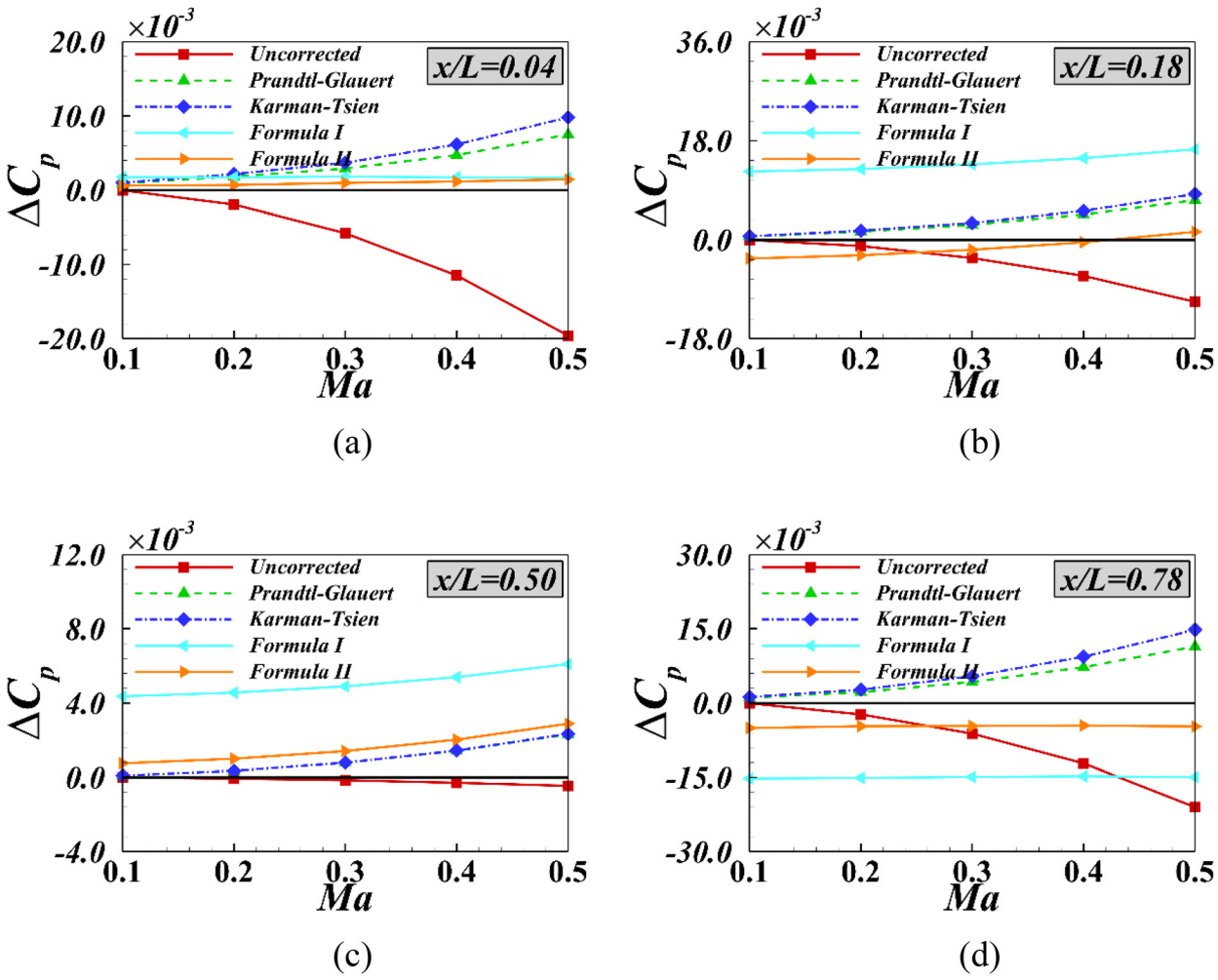

FIG. 13. Differences in pressure coefficient corrected by different formulas with varying *Ma*: (a) $x/L = 0.04$; (b) $x/L = 0.18$; (c) $x/L = 0.5$; and (d) $x/L = 0.78$. *Formula I*—results of CF-I; *Formula II*—results of CF-II; solid black line—baseline for ideal case of $\Delta C_p = 0$.

correction term contains pressure coefficient, which is similar to the Karman–Tsien rule. The correction term containing the pressure coefficient nonlinearized the formula, which is the important factor for the Karman–Tsien rule at higher Mach number. In a sense, the proposed formula has the correction characteristics of both the Prandtl–Glauert rule and the Karman–Tsien rule, and thus obtained the correction characteristics at both low and high Mach number.

V. CONCLUSION

We proposed finite-wing-analogy formulas for compressibility correction to the SUBOFF pressure coefficient at low Mach number. Inspired by the finite-wing correction for the lift slope of airfoils, we developed two finite-wing-analogy formulas (CF-I and CF-II) and evaluated them in comparison with the Prandtl–Glauert rule, the Karman–Tsien rule, and the Laitone rule, these being the three compressibility correction formulas that are used most widely. The SUBOFF flow field was obtained by solving the RANS equations for compressible flow numerically, with the Mach number based on the freestream velocity varying from 0.004 to 0.5. The average correction factor was used to measure the convergence ability of each formula regarding the pressure-coefficient curve at different Mach numbers, and the pressure-coefficient difference was used to evaluate the error of compressibility correction. It was found that the proposed formulas offer better convergence than the widely used correction formulas. CF-I has a simple form and offers good convergence of the pressure coefficient, but its pressure-coefficient difference between compressible and incompressible flow is relatively large. By contrast, CF-II offers both good convergence and good compressibility correction of the pressure coefficient. Therefore, the proposed CF-II can be used to convert the pressure coefficient between measurements in a wind tunnel and those in a water tunnel or towing tank.

ACKNOWLEDGMENTS

This work was supported by the NSFC Basic Science Center Program for Multiscale Problems in Nonlinear Mechanics (Grant

08 April 2024 03:18:05

Published under an exclusive license by AIP Publishing

No. 11988102), the National Natural Science Foundation of China (Grant Nos. 12102439, 11922214, and 91952301), and the Pilot National Laboratory for Marine Science and Technology (Qingdao, Wenhai Project No. 2021WHZZB1400). The computations were conducted on Tianhe-1 at the National Supercomputer Center in Tianjin. We would like to thank the reviewers for their constructive comments. We are grateful to Ting Wu and Yongtao Wang for their helpful discussion.

AUTHOR DECLARATIONS

Conflict of Interest

The authors have no conflicts of interest to disclose.

Author Contributions

Yu Wang: Data curation (equal); Formal analysis (equal); Methodology (equal); Validation (equal); Visualization (equal); Writing – original draft (equal); Writing – review & editing (equal). **Yi Liu:** Data curation (equal); Methodology (equal); Software (lead); Writing – review & editing (equal). **Zhiteng Zhou:** Data curation (equal). **Shizhao Wang:** Conceptualization (lead); Funding acquisition (supporting); Supervision (lead); Writing – original draft (equal); Writing – review & editing (equal).

DATA AVAILABILITY

The data that support the findings of this study are available from the corresponding author upon reasonable request.

APPENDIX A: UNCERTAINTY ANALYSIS

In the present study, the Mach number is the only source of the uncertainty and is treated as an uncertain variable. Then, we use the non-intrusive probabilistic collocation polynomial chaos (NIPC) method to quantify the uncertainty of the pressure coefficient in terms of the Mach number. The NIPC obtains the statistical properties of uncertain variables by deterministic calculation results. Since the NIPC established the relationship between input and output parameters without any modification of the CFD solver, it has been widely used in uncertainty analysis with CFD.

The non-intrusive probabilistic collocation method[80] (NIPRC) employed Lagrangian polynomials to obtain polynomial chaos with random variables, which are approximated with the polynomial chaos expansion

$$\psi(x,\xi^*) \approx \sum_{i=0}^{N_P} \psi_i(x) L_i(\xi^*). \tag{A1}$$

Here, $\psi_i(x)$ is the deterministic expansion coefficients corresponding to the ith mode, which can be obtained by the CFD solution at collocation points υ_i. N_p is the number of collocation points. The term $L_i(\xi^*)$ is Lagrangian polynomial chaos expansion in the vector of random variables $\xi^*(\upsilon)$, which can be given by

$$L_i(\xi^*(\upsilon)) = \prod_{\substack{j=1 \\ j\neq i}}^{N_p} \frac{\xi^*(\upsilon) - \xi^*(\upsilon_j)}{\xi^*(\upsilon_i) - \xi^*(\upsilon_j)}, \tag{A2}$$

where υ is the fundamental event on the sample space. The Lagrange interpolating polynomial chaos is the polynomial chaos of order $N_p - 1$ that passes through the N_p collocation points. A powerful method to compute Gaussian quadrature rules is by means of the Golub–Welsch algorithm.[81] The mean and variance of the solution are found by

$$\mu_\psi = \sum_{i=0}^{N_P} \psi_i(x)\omega_i, \tag{A3}$$

$$\sigma_\varphi^2 = \sum_{i=0}^{N_P} \left[\left(\psi_i(x) - \mu_\psi\right)^2 \right] \omega_i, \tag{A4}$$

where ω_i are the weights corresponding to the collocation points.

In the present work, the Mach number is assumed to subject to the normal distribution with the mean value is $\mu_{Ma} = 0.3$ and the variance is $\sigma_{Ma}^2 = 2 \times 10^{-4}$. The collocation points for the two-order NIPRC method are shown in Table V. The table also lists the corresponding numerical results, including the lift coefficient and drag coefficient. With containing 95% of all possible values, Fig. 14 shows the pressure coefficient with the uncertainty bars indicating the interval. It can be seen in Fig. 14, the uncertainty of the Mach number has an extremely weak effect on the pressure coefficient, and the maximum value of the uncertainty band is about 0.0012.

TABLE V. The two-order probabilistic collocate points and corresponding weights.

Point number	*Ma*	Weights
1	0.282 68	0.166 67
2	0.300 00	0.666 67
3	0.317 32	0.166 67

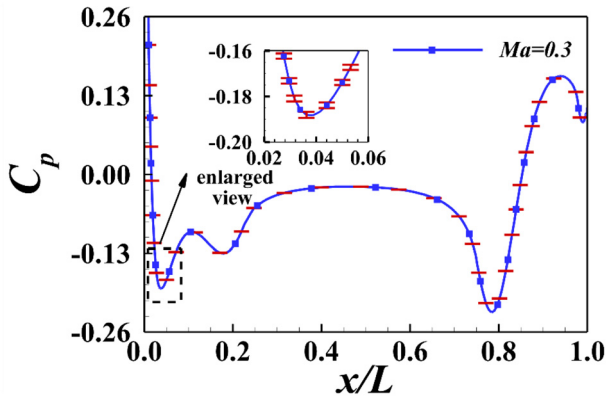

FIG. 14. The mean pressure coefficient with the uncertainty bars indicating the interval, which contains 95% of all possible values. The variations in pressure coefficient are caused by the uncertainty of Mach number.

APPENDIX B: THE SIMILARITY RULES FOR LINEARIZED AXIALLY SYMMETRIC FLOW AND PLANAR FLOW

As one of the similarity rules, the Prandtl–Glauert rule has the widest application. However, there are two other similarity rules of high speed flow for linearized axially symmetric flow and planar

08 April 2024 03:18:05

Published under an exclusive license by AIP Publishing

flow, which can also be used to correct the pressure coefficient of SUBOFF. Similar to the Prandtl–Glauert rule, the similarity rules of high speed flow for linearized axially symmetric flow and planar flow establish the transformation between two similar flows by assuming the relationship between linearized perturbation potential functions and the relationship between the two coordinate systems.

For axially symmetric flow, the conversion of pressure coefficient of compressible flow and incompressible flow can be given as

$$C_{p,0} = AC_p, \tag{B1}$$

where the $C_{p,0}$ and C_p represent the pressure coefficient of incompressible flow and compressible flow, respectively. The parameter A is determined by the relation

$$A = \frac{1 - Ma_2^2}{1 - Ma_1^2}, \tag{B2}$$

where Ma_1 and Ma_2 are the Mach number of incompressible flow and compressible flow, respectively. Different to the formulas in the manuscript, there is an additional condition for Eqs. (B1) and (B2), given as

$$D = D_0\sqrt{\frac{1 - Ma_1^2}{1 - Ma_2^2}}, \tag{B3}$$

where D_0 and D are the maximum diameter of the SUBOFF model of incompressible flow and compressible flow, respectively. Hence, the conversion of the pressure coefficient is no longer related only to the Mach number, but also to the maximum diameter of SUBOFF.

Since Kármán[60] considers result of $Ma = 0.1$ as incompressible flow data with the term $1 - Ma_1^2$ very close to 1. We have calculated the maximum differences of pressure coefficients for $Ma \leq 0.1$ and $Ma \geq 0.1$ are 0.4×10^{-2} and 6.5×10^{-2}, respectively. Therefore, we also considered $Ma_1 = 0.1$ as incompressible flow to match the form of the formulas in the manuscript. Based on this, Eqs. (B2) and (B3) can be simplified as

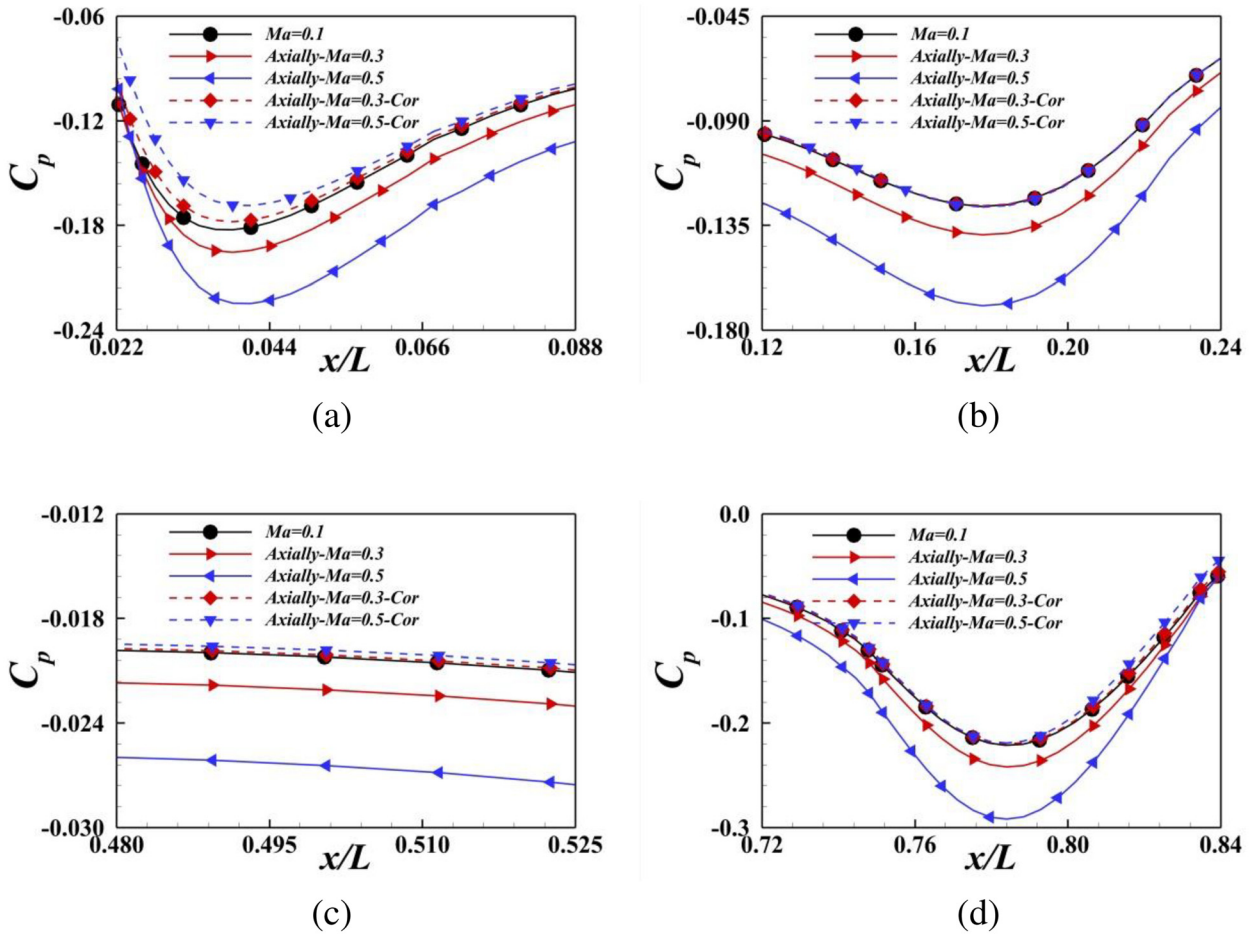

FIG. 15. Corrected results of the similarity rule of linear axially symmetric flow for pressure coefficients at typical SUBOFF locations: (a) $x/L = 0.04$; (b) $x/L = 0.18$; (c) $x/L = 0.5$; and (d) $x/L = 0.78$. The solid lines represent the pressure coefficient at different Mach numbers without correction, and the dashed lines represent the corrected pressure coefficient of correction formula.

08 April 2024 03:18:05

Published under an exclusive license by AIP Publishing

$$A = 1 - Ma, \tag{B4}$$

and

$$D = D_0\sqrt{\frac{1}{1 - Ma}}. \tag{B5}$$

Here, D_0 can be considered as the diameter of the SUBOFF without scaling, D is the scaling one, and Ma is the Mach number of compressible flows. We employed the above conversion to the pressure coefficient for $Ma = 0.3$ and $Ma = 0.5$. As shown in Fig. 15, the similarity rule of linear axially symmetric flow provides a good agreement for the correction of the hull at the selected typical locations of $x/L = 0.18$, $x/L = 0.5$, and $x/L = 0.78$. The typical location at $x/L = 0.04$ is close to the top of the hull, and the radius tends to be 0. The boundary conditions cannot be satisfied here, which may be the reason for the larger error at this location.

Then, we will numerically compare the correction results of this formula with others. The overall correction effect of the formula is quantified by the average correction factor ξ, which is defined as

$$\xi = 1 - \frac{\overline{\eta_{cor}}}{\overline{\eta_{uncor}}}, \tag{B6}$$

where $\overline{\eta_{uncor}}$ is the average of the compressibility error without correction, and $\overline{\eta_{cor}}$ represents that of corrected results. For similarity rule of axially symmetric flow, it is worth noting that the pressure coefficient without correction is the simulation result of scaling shape of SUBOFF model, as shown in Eqs. (B1) and (B5). Since the compressibility error with corrected is the quantity with more concern, the value of uncorrected compressibility errors should be the same as the origin one, which are $\eta_{uncor,a} = 8.85\%$, $\eta_{uncor,b} = 5.51\%$, $\eta_{uncor,c} = 0.20\%$, and $\eta_{uncor,d} = 9.48\%$, respectively. The value of corrected compressibility errors should be redefined as

$$\eta_{cor} = \frac{|C_{p,Ma=0.5} - C_{p,Ma=0.1}|_{cor,D}}{|C_{p,Ma=0.1,\min}|_{D_0}}. \tag{B7}$$

With Eq. (B7), the obtained corrected compressibility errors at typical locations are $\eta_{cor,a} = 6.40\%$, $\eta_{cor,b} = 0.13\%$, $\eta_{cor,c} = 0.18\%$, and $\eta_{cor,d} = 0.93\%$, respectively. Substituting the above data into Eq. (B6), the average correction factor of similarity rules for linear

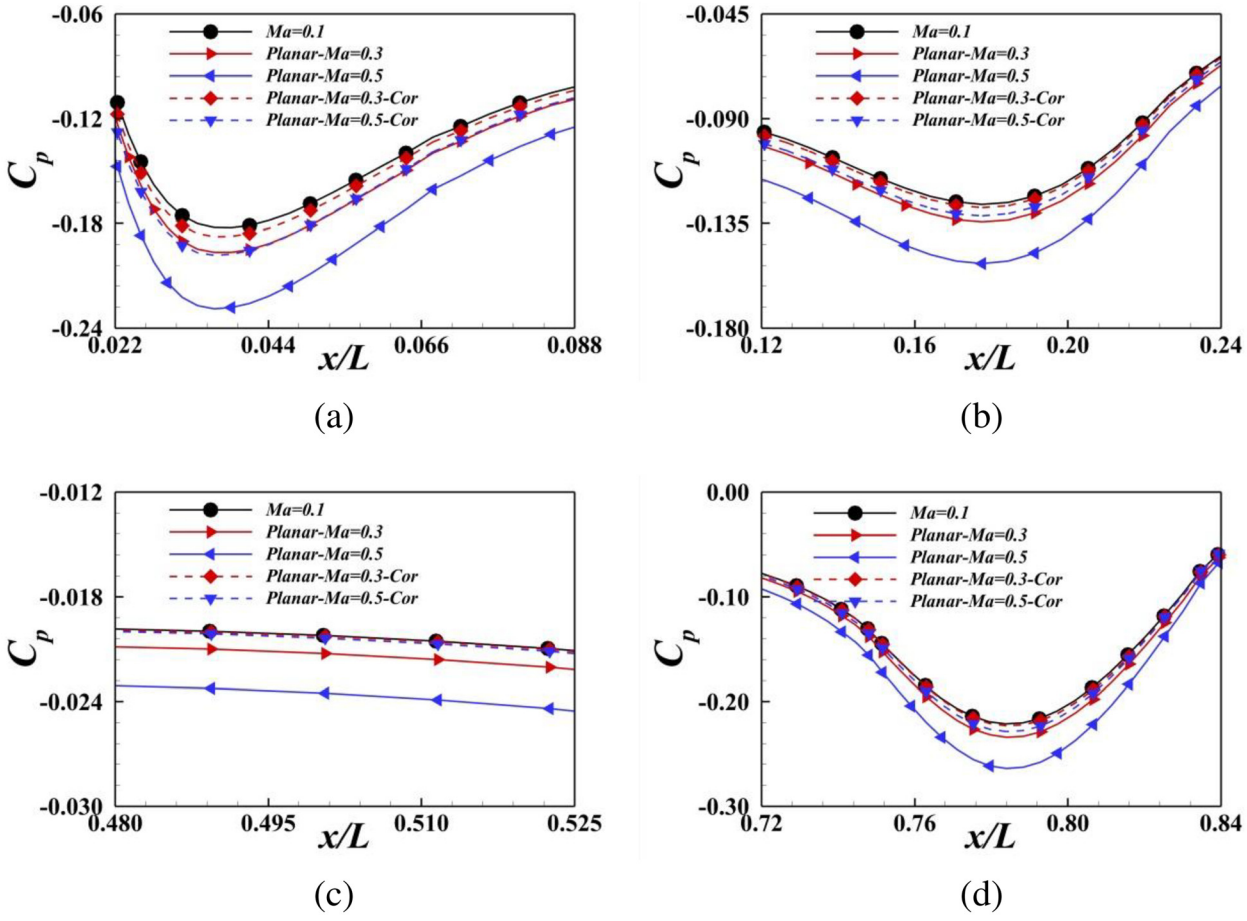

FIG. 16. Corrected results of the similarity rule of planar flow for pressure coefficients at typical SUBOFF locations: (a) $x/L = 0.04$; (b) $x/L = 0.18$; (c) $x/L = 0.5$; and (d) $x/L = 0.78$.

08 April 2024 03:18:05

Published under an exclusive license by AIP Publishing

axially symmetric flow is $\xi_{S-AS} = 0.68$. The average correction factors of proposed formula are $\xi_{For-I} = 0.88$ and $\xi_{For-II} = 0.84$, respectively. The similarity rules for the subsonic flow were derived from the small perturbation theory for potential flow under the conditions of planar/slender bodies with a small angle of attack. Therefore, linear axially symmetric rule can get the best correction at point b to d on the straight section of SUBOFF. However, location a is close to the stationary point where the flow does not satisfy the assumption of small perturbation, resulting in large errors when the similarity rule of linear axially symmetric flow is used. We would also like to point out that the improvements of the proposed formulas CF-I [Eq. (31)] and CF-II [Eq. (45)] are made by numerical fitting. In particular, if Mach number is set to 0.1 in Eq. (31), the pressure coefficient $C_{p,0}$ is not always equal to the right hand due to the introduction of low aspect ratio correction.

For planar flow, the conversion of pressure coefficient of compressible flow and incompressible flow can be given as

$$C_{p,0} = AC_p. \tag{B8}$$

Here, the parameter A is related to the shape of the hull, giving the equation

$$A = \frac{D_{z1}}{D_{z2}}\sqrt{\frac{1 - Ma_2^2}{1 - Ma_1^2}}, \tag{B9}$$

where D_{z1} and D_{z2} are the scaling diameters in the z direction corresponding to Ma_1 and Ma_2, respectively. There is an additional shape scaling with

$$\frac{D_{y1}}{D_{y2}} = \sqrt{\frac{1 - Ma_2^2}{1 - Ma_1^2}}, \tag{B10}$$

where D_{y1} and D_{y2} are the scaling diameters in the z direction corresponding to Ma_1 and Ma_2, respectively. Similarly, Eqs. (B9) and (B10) can be simplified with considering $Ma_1 = 0.1$ as incompressible flow. The above conversion is adopted to the pressure coefficient for $Ma = 0.3$ and $Ma = 0.5$. As shown in Fig. 16, the correction effect of similarity rule of planar flow is slightly worse than the similarity rule of linear axially symmetric flow. The correction error at the location $x/L = 0.04$ is larger than other locations, as well. Numerically, the corrected compressibility errors at typical locations are $\eta_{uncor,a} = 6.86\%$, $\eta_{uncor,b} = 2.25\%$, $\eta_{uncor,c} = 0.07\%$, and $\eta_{uncor,d} = 3.32\%$, respectively. The average correction factor of similarity rule of planar flow is $\xi_{S-P} = 0.47$. According to the average correction factor ξ and the compressibility error η, the proposed formula performs better in compressibility correction for the pressure coefficient of SUBOFF. Although the similarity rules of linearized axially symmetric flow and planar flow demonstrate a good compressibility correction in some locations, the diameter changes with the Mach number. This makes it difficult to be applied effectively in experiments.

REFERENCES

[1]A. Posa and E. Balaras, "A numerical investigation about the effects of Reynolds number on the flow around an appended axisymmetric body of revolution," J. Fluid Mech. **884**, A41 (2020).

[2]T. T. Huang, H. L. Liu, N. C. Grooves, T. J. Forlini, J. N. Blanton, and S. Gowing, "Measurements of flows over an axisymmetric body with various appendages in a wind tunnel: The DARPA SUBOFF experimental program," in *Proceedings of the 19th Symposium on Naval Hydrodynamics* (National Academy Press, Seoul, South Korea, 1994), p. 321.

[3]R. F. Roddy, "Investigation of the stability and control characteristics of several configurations of the DARPA SUBOFF model (DTRC model 5470) from captive-model experiments," Report No. DTRC/SHD-1298-08 (David Taylor Research Center Bethesda MD Ship Hydromechanics Dept, 1990).

[4]H. L. Liu, C. W. Jiang, D. J. Fry, and M. S. Chang, "Installation and pretest analysis of DARPA SUBOFF model in the DTRC anechoic wind tunnel," Report No. DTRC/SHD-1298-04 (David Taylor Research Center Bethesda MD Ship Hydromechanics Dept, 1990).

[5]A. Ashok, B. T. Van, and A. J. Smits, "Asymmetries in the wake of a submarine model in pitch," J. Fluid Mech. **774**, 416–442 (2015).

[6]J. M. Jiménez, M. Hultmark, and A. J. Smits, "The intermediate wake of a body of revolution at high Reynolds numbers," J. Fluid Mech. **659**, 516–539 (2010).

[7]J. M. Jiménez, R. T. Reynolds, and A. J. Smits, "The effects of fins on the intermediate wake of a submarine model," J. Fluids Eng. **132**, 031102 (2010).

[8]R. Kowalyshyn, "Resistance and static planar motion mechanism tests for DTRC model 5470," Report No. 88006 10-1 (Tracor Hydronautics, 1990).

[9]J. N. Blanton, T. J. Forlini, and L. P. Purtell, "Hot-film velocity measurement uncertainty for DARPA (defense advanced research projects agency) SUBOFF experiment," Report No. DTRC/SHD-1298-05 (David Taylor Research Center Bethesda MD Ship Hydromechanics Department, 1990).

[10]S. Gowing, "Pressure and shear stress measurement uncertainty for DARPA (defense advanced research projects agency) SUBOFF experiment," Report No. DTRC/SHD-1298-06 (David Taylor Research Center Bethesda MD Ship Hydromechanics Department, 1990).

[11]C. W. Jiang, H. L. Liu, and T. T. Huang, "Determination of wind tunnel wall effects and corrections," in *Proceeding of the 19th International Towing Tank Conference* (ITTC, 1990), pp. 310–317.

[12]S. Hosder and R. L. Simpson, "Experimental investigation of unsteady flow separation on a maneuvering axisymmetric body," J. Aircr. **44**, 1286–1295 (2007).

[13]A. Ashok, T. V. Buren, and A. J. Smits, "The structure of the wake generated by a submarine model in yaw," Exp. Fluids **56**, 123 (2015).

[14]Y. H. Lin, S. H. Tseng, and Y. H. Chen, "The experimental study on maneuvering coefficients of a submerged body SUBOFF by implementing the planar motion mechanism tests," Ocean. Eng. **170**, 120–135 (2018).

[15]X. Y. Liang, N. Ma, H. Liu, and X. C. Gu, "Experimental study on the maneuvering derivatives of a half-scale SUBOFF model in the vertical plane," Ocean. Eng. **233**, 109052 (2021).

[16]Y. Liu, Z. Yu, L. Zhang, T. Liu, D. Feng, and J. Zhang, "A fine drag coefficient model for hull shape of underwater vehicles," Ocean. Eng. **236**, 109361 (2021).

[17]M. K. Khan, M. Korulla, V. Nagarajan, and O. P. Sha, "Surface pressure measurements on a generic submarine hull form at high angles of incidence," J. Mar. Sci. Technol. **27**, 677–694 (2022).

[18]L. P. Erm, *An Assessment of the Usefulness of Water Tunnels for Aerodynamic Investigations* [Defence Science and Technology Organisation Victoria (Australia) Air Vehicles DIV, 2012].

[19]D. Papamoschou and A. Roshko, "The compressible turbulent shear layer: An experimental study," J. Fluid Mech. **197**, 453–477 (1988).

[20]S. Sarkar, "The stabilizing effect of compressibility in turbulent shear flow," J. Fluid Mech. **282**, 163–186 (1995).

[21]C. Pantano and S. Sarkar, "A study of compressibility effects in the high-speed turbulent shear layer using direct simulation," J. Fluid Mech. **451**, 329–371 (2002).

[22]H. Foysi, S. Sarkar, and R. Friedrich, "Compressibility effects and turbulence scalings in supersonic channel flow," J. Fluid Mech. **509**, 207–216 (2004).

[23]S. J. Beresh, J. L. Wangner, and K. M. Casper, "Compressibility effects in the shear layer over a rectangular cavity," J. Fluid Mech. **808**, 116–152 (2016).

[24]B. Yang, G. Jin, T. Wu, Z. Yang, and G. He, "Numerical implementation and evaluation of resolvent-based estimation for space–time energy spectra in turbulent channel flows," Acta Mech. Sin. **36**, 775–788 (2020).

[25]Y. Song, C. Xu, W. Huang, and L. Wang, "Transient growth in turbulent particle-laden channel flow," Acta Mech. Sin. **36**, 1–11 (2020).

08 April 2024 03:18:05

Published under an exclusive license by AIP Publishing

[26]X. J. Zheng and G. H. Wang, "Progresses and challenges of high Reynolds number wall-bounded turbulence," Adv. Mech. **50**, 202001 (2020).
[27]Y. Dong and G. He, "Scaling of energy spectra in weakly compressible turbulence," Acta Mech. Sin. **33**, 500–507 (2017).
[28]J. C. Wang, Y. P. Shi, L. P. Wang, Z. L. Xiao, X. T. He, and S. Y. Chen, "Effect of compressibility on the small scale structures in isotropic turbulence," J. Fluid Mech. **713**, 588–631 (2012).
[29]J. C. Wang, M. P. Wan, S. Chen, and S. Y. Chen, "Kinetic energy transfer in compressible isotropic turbulence," J. Fluid Mech. **841**, 581–613 (2018).
[30]Z. Yuan, Y. Wang, C. Xie, and J. Wang, "Deconvolutional artificial-neural-network framework for subfilter-scale models of compressible turbulence," Acta Mech. Sin. **37**, 1773–1785 (2021).
[31]C. Y. Xie, J. C. Wang, H. Li, M. P. Wan, and S. Y. Chen, "Artificial neural network mixed model for large eddy simulation of compressible isotropic turbulence," Phys. Fluids **31**, 085112 (2019).
[32]Z. Jiang, Y. Ji, and J. Wang, "Compressibility effect on interaction of shock wave and turbulent boundary layer," Phys. Fluids **34**, 075122 (2022).
[33]S. Nilsson, H. D. Yao, A. Karlsson, and S. Arvidson, "Effects of viscosity and density on the aeroelasticity of the ONERA M6 wing from subsonic to supersonic speeds," in *AIAA AVIATION Forum* (AIAA, 2022).
[34]M. Yu and C. X. Xu, "Compressibility effects on hypersonic turbulent channel flow with cold walls," Phys. Fluids **33**, 075106 (2021).
[35]R. Z. Yang, R. Yang, and Y. X. Zhao, "Influence of compressibility on the development of streamwise supersonic corner flow," Phys. Fluids **33**, 116102 (2021).
[36]K. Karantonis, I. W. Kokkinakis, B. Thornber, and D. Drikakis, "Compressibility in suddenly expanded subsonic flows," Phys. Fluids **33**, 105106 (2021).
[37]D. W. Moore and D. I. Pullin, "The compressible vortex pair," J. Fluid Mech. **185**, 171–204 (1987).
[38]D. W. Moore and D. I. Pullin, "The vortex pair in a compressible ideal gas," Fluid Dyn. Res. **3**, 377 (1988).
[39]S. C. Crow, "Stability theory for a pair of trailing vortices," AIAA J. **8**, 2172–2179 (1970).
[40]S. E. Widnall, D. Bliss, and A. Zalay, "Theoretical and experimental study of the stability of a vortex pair," in *Aircraft Wake Turbulence and Its Detection* (Plenum, 1971), pp. 305–338.
[41]P. G. Saffman and G. R. Baker, "Vortex interactions," Annu. Rev. Fluid Mech. **11**, 95–121 (1979).
[42]D. I. Meiron and D. I. Pullin, "On steady compressible flows with compact vorticity; The compressible Hill's spherical vortex," J. Fluid Mech. **374**, 285–303 (1998).
[43]D. I. Meiron, D. W. Moore, and D. I. Pullin, "On steady compressible flows with compact vorticity; the compressible Stuart vortex," J. Fluid Mech. **409**, 29–49 (2000).
[44]S. D. Heister, J. M. Mcdonough, A. R. Karagozian, and D. W. Jenkins, "The compressible vortex pair," J. Fluid Mech. **220**, 339–354 (1990).
[45]N. D. Sandham, "The effect of compressibility on vortex pairing," Phys. Fluids **6**, 1063–1072 (1994).
[46]D. G. Crowdy and V. S. Krishnamurthy, "Speed of a von Kármán point vortex street in a weakly compressible fluid," Phys. Rev. Fluids **2**, 114701 (2017).
[47]H. Lin, Y. Xiang, H. Xu, H. Liu, and B. Zhang, "Passive scalar mixing induced by the formation of compressible vortex rings," Acta Mech. Sin. **36**, 1258–1274 (2020).
[48]F. Feng, X. Meng, L. Guo, and Q. Wang, "Directivity of acoustic field generated by leapfrogging vortices," Phys. Fluids **32**, 126106 (2020).
[49]L. Guo, J. Lv, F. Feng, and Q. Wang, "CFD verification and weak compressibility correction of unsteady aerodynamic force models applied to high-amplitude oscillating incoming flows," Acta Aerodyn. Sin. **35**, 93–100 (2017).
[50]K. V. Rozhdestvensky, "Wing-in-ground effect vehicles," Prog. Aerosp. Sci. **42**, 211–283 (2006).
[51]H. Mukohara and M. Anyoji, "Computational analysis of compressibility effect on flow field and aerodynamics at low Reynolds numbers," Phys. Fluids **34**, 056109 (2022).
[52]A. R. Teymourtash and S. E. Salimipour, "Compressibility effects on the flow past a rotating cylinder," Phys. Fluids **29**, 016101 (2017).
[53]D. H. Wood, "Some effects of compressibility on small horizontal-axis wind turbines," Renewable Energy **10**, 11–17 (1997).
[54]D. Canuto and K. Taira, "Two-dimensional compressible viscous flow around a circular cylinder," J. Fluid Mech. **785**, 349–371 (2015).
[55]T. Colonius, S. K. Lele, and P. Moin, "The free compressible viscous vortex," J. Fluid Mech. **230**, 45–73 (1991).
[56]H. Glauert, "The effect of compressibility on the lift of an aerofoil," Proc. R. Soc. London, Ser. A **118**, 113–119 (1928).
[57]H. Glauert, *The Elements of Aerofoil and Airscrew Theory* (The University Press, 1926).
[58]E. V. Laitone, "New compressibility correction for two-dimensional subsonic flow," J. Aeronaut. Sci. **18**, 350–350 (1951).
[59]H. S. Tsien, "Two-dimensional subsonic flow of compressible fluids," J. Spacecr. Rockets **40**, 983–991 (2003).
[60]T. V. Kármán, "Compressibility effects in aerodynamics," J. Aeronaut. Sci. **8**, 337–365 (1941).
[61]T. Nagata, A. Noguchi, K. Kusama, T. Nonomura, A. Komuro, A. Ando, and K. Asai, "Experimental investigation on compressible flow over a circular cylinder at Reynolds number of between 1000 and 5000," J. Fluid Mech. **893**, A13 (2020).
[62]C. Yan and C. L. Archer, "Assessing compressibility effects on the performance of large horizontal-axis wind turbines," Appl. Energy **212**, 33–45 (2018).
[63]N. Balin, F. Casenave, F. Dubois, E. Duceau, S. Duprey, and I. Terrasse, "Boundary element and finite element coupling for aeroacoustics simulations," J. Comput. Phys. **294**, 274–296 (2015).
[64]J. Kirkman and T. Takahashi, "Revisiting the transonic similarity rule: Critical Mach number prediction using potential flow solutions," in *34th AIAA Applied Aerodynamics Conference* (AIAA, 2016).
[65]A. Kontogiannis and E. Laurendeau, "Adjoint state of nonlinear vortex-lattice method for aerodynamic design and control," AIAA J. **59**, 1184–1195 (2021).
[66]Z. M. Xu, Z. H. Han, and W. P. Song, "An improved 2.75 D method relating pressure distributions of 2D airfoils and 3D wings," Aerosp. Sci. Technol. **128**, 107789 (2022).
[67]S. Su, X. Shan, P. Yu, and H. Wang, "The compressibility effects on the inherent stability of wing-in-ground crafts," in *AIAA SCITECH Forum* (AIAA, 2022), p. 2572.
[68]N. P. Werter, R. D. Breuker, and M. M. Abdalla, "Continuous-time state-space unsteady aerodynamic modeling for efficient loads analysis," AIAA J. **56**, 905–916 (2018).
[69]N. C. Groves, T. T. Huang, and M. S. Chang, "Geometric characteristics of DARPA (defense advanced research projects agency) SUBOFF models (DTRC model numbers 5470 and 5471)," Report No. DTRC/SHD-1298-01 (David Taylor Research Center Bethesda MD Ship Hydromechanics Department, 1989).
[70]T. B. Gatski and J. P. Bonnet, *Compressibility, Turbulence and High Speed Flow*, 2nd ed. (Academic Press, 2013), Chap. 3.
[71]F. R. Menter, "Two-equation eddy-viscosity turbulence models for engineering applications," AIAA J. **32**, 1598–1605 (1994).
[72]Y. Liu, G. Wang, and Z. Ye, "Dynamic mode extrapolation to improve the efficiency of dual time stepping method," J. Comput. Phys. **352**, 190–212 (2018).
[73]Y. Liu, "Turbulence modeling and its uncertainty quantification for complex aerodynamic flows," Ph.D. thesis (Northwestern Polytechnical University, 2020).
[74]Y. Liu, Z. Zhou, L. Zhu, and S. Wang, "Numerical investigation of flows around an axisymmetric body of revolution by using Reynolds-stress model based hybrid Reynolds-averaged Navier–Stokes/large eddy simulation," Phys. Fluids **33**, 085115 (2021).
[75]S. Yoon and A. Jameson, "Lower-upper symmetric-Gauss-Seidel method for the Euler and Navier-Stokes equations," AIAA J. **26**, 1025–1026 (1988).
[76]A. Posa and E. Balaras, "A numerical investigation of the wake of an axisymmetric body with appendages," J. Fluid Mech. **792**, 470–498 (2016).
[77]J. Anderson, *Fundamentals of Aerodynamics*, 6rd ed. (McGraw-Hill, 2011) pp.750–755.
[78]R. Vos and S. Farokhi, *Introduction to Transonic Aerodynamics* (Spring, 2015), Vol. 110.
[79]H. W. Liepmann and A. Roshko, *Elements of Gasdynamics* (Wiley, New York, 1957).
[80]G. J. A. Loeven, J. A. S. Witteveen, and H. Bijl, "Probabilistic collocation: An efficient non-intrusive approach for arbitrarily distributed parametric uncertainties," in *45th AIAA Aerospace Sciences Meeting and Exhibit* (AIAA, 2007), p. 317.
[81]G. H. Golub and J. H. Welsch, "Calculation of Gauss quadrature rules," Math. Comput. **23**, 221–230 (1969).

08 April 2024 03:18:05

Published under an exclusive license by AIP Publishing